Coherence–Rupture–Regeneration: a geometric framework for temporal variability tested across neural oscillations and 132 oscillatory systems

Alexander Sabine

Abstract

All finite systems that persist through time must accumulate coherent patterns, reach the limits of their current regime, and reconstruct from their own history. We propose that for oscillatory systems, this temporal process may be governed by a single geometric parameter determined by the topology of the system's state space. We present the Coherence–Rupture–Regeneration (CRR) framework, in which the boundary between a system's past and future is co-constructed at the moment the Cramér–Rao bound is saturated ($C \cdot \Omega = 1$), yielding a prediction for the coefficient of variation of inter-event intervals without fitted parameters. Two fundamental symmetry classes, bistable and rotational, predict distinct variability baselines with a predicted ratio of two.

The CV prediction $\Omega/2$ is derived from five axioms: the three CRR equations select an exponential family on the statistical manifold, the maximum-entropy principle fixes the operating point, and the Dirac delta in the rupture equation fixes the effective sample size to exactly one. This entails that CV scales linearly with Ω—not as $\sqrt{\Omega}$—a prediction empirically distinguishable from standard first-passage alternatives and confirmed across 45 autonomous systems ($\Delta\text{AIC} = 1{,}445$).

Tested across 298 subjects in two independent EEG datasets and 132 independently classified oscillatory systems spanning 20 domains, the predicted structure is supported with zero directional reversals. We offer this framework as a candidate temporal grammar with cross-domain evidence.

1 Introduction

All systems transform through time, but some systems transform through time differently to others. A heart does not beat with metronomic regularity. A star does not pulsate in perfectly even intervals. A neuron fires, rests, and fires again, never quite the same way twice. This temporal variability—measured as the coefficient of variation (CV) of inter-event intervals—is typically treated as noise to be averaged away [24, 25]. We propose that it is a signal, and that its value is determined by geometry.

The observation motivating this proposal is empirical and, to us, unexpected. Across a wide range of oscillatory systems—from calcium signalling in hepatocytes [45] to the glacial-interglacial cycle [54], from cardiac rhythms [43] to candle flame flicker, from chick somitogenesis [49] to yeast glycolytic oscillations [48]—the CV of inter-event intervals clusters around two values: approximately 0.16 and approximately 0.08. These systems share no obvious physical mechanism. What they share is a topological feature: systems near 0.16 alternate between two distinguishable states (bistable dynamics), while systems near 0.08 traverse a continuous cycle (rotational dynamics). The ratio between these clusters is close to 2.

This clustering is difficult to explain within standard stochastic frameworks. Near a Hopf bifurcation, stochastic limit-cycle theory [25] gives CV $\propto D^{1/2}/\mu$, with two continuously adjustable parameters. A drift-diffusion model predicts CV $= \sigma/\mu$, again freely adjustable. Neither framework explains why autonomous oscillators across domains should converge on specific values determined by topology, nor why the ratio between classes should be integer-valued. If CV is a free parameter, the clustering is a coincidence. We propose it is not.

The question this paper addresses is general: what constrains the temporal variability of a finite system? Any system that persists must accumulate patterns that work. Any finite system must eventually exhaust its current regime. After exhaustion, it must reconstruct from its own history. We argue that these three temporal operations—accumulation, transition, reconstruction—describe something that neurons, hearts, chemical oscillators, ecological cycles, and engineered timekeepers all do, despite having nothing else in common. A claim this broad requires correspondingly broad evidence, and we are aware that cross-domain universality claims have a mixed track record in science. We therefore present CRR not as a proven law but as a candidate framework with specific, falsifiable predictions, tested across enough domains that the pattern, if it is real, should be visible—and if it is not, should fail conspicuously.

1.1 A temporal gap in the Free Energy Principle

The Free Energy Principle (FEP) [11, 15] provides a powerful account of how self-organising systems maintain their statistical boundaries. Under the FEP, a system persists by minimising variational free energy—the discrepancy between its generative model and the sensory evidence it encounters. Central to this account is the Markov blanket [10]: the statistical boundary that separates internal states from external states, through which all interaction is mediated. The FEP describes how this blanket works: how internal states come to parametrise beliefs about external states and how the system acts to reduce surprise.

What the FEP does not yet provide is an account of when and how this blanket reconfigures. The spatial Markov blanket persists at steady state [10], but real systems are not at steady state forever. They undergo phase transitions: a neuron fires, a cell divides, an ecosystem reorganises after a disturbance. These transitions involve the reconfiguration of the very boundary the FEP describes. CRR proposes a candidate account of this temporal reconfiguration.

The central claim is that whenever a system minimises free energy, it is building what we call *coherence*: the integral of its past states. But a finite system cannot accumulate coherence without bound. At some point—formalised as the saturation of the Cramér–Rao bound [7, 8]—the current regime is exhausted and the system must reorganise. CRR asks: when does this reorganisation happen, and what does the system do afterward?

The answers, we propose, are governed by a single geometric parameter, Ω, fixed by the topology of the system's state space. Ω simultaneously determines how much coherence can accumulate before reorganisation, how often the system must reorganise, and which moments from the past matter most for reconstruction. These are not three independent properties; they are a single geometric fact. If this account is correct, it extends the FEP from a theory of how systems maintain their boundaries to a theory of when those boundaries must reconfigure—a temporal complement to the spatial Markov blanket.

We are mindful of recent discussions regarding the empirical scope and falsifiability of broad theoretical frameworks [26, 27]. CRR is designed to address this concern directly. The framework predicts two specific numbers ($1/(2\pi)$ and $1/(4\pi)$), a specific ratio (predicted to be 2), and a directional structure (the three-class framework of Section 2.4). Any directional reversal—a regulated system appearing above the geometric baseline, or a noise-dominated system appearing below it—falsifies the account of Ω as governing reconstruction breadth. The pre-registration protocol (Appendix A) is domain-general: any researcher can classify a system, register a prediction, and test it.

1.2 Mathematical foundations

The derivation connects four results of independent standing in information geometry, estimation theory, and statistical mechanics. Čencov's uniqueness theorem [5, 6] establishes the Fisher information metric as the unique reparametrisation-invariant Riemannian metric on statistical manifolds—the natural arena for describing systems that parametrise probability distributions [1, 2]. The Cramér–Rao bound [3, 4] provides the fundamental lower limit on estimation precision. Ito and Dechant [7] extended this bound rigorously to stochastic time evolution on statistical manifolds, and Nicholson *et al.* [8] established a family of time-information uncertainty relations mirroring the Mandelstam–Tamm relation, demonstrating that thermodynamic fluctuation timescales are universally bounded by the Fisher information. Da Costa *et al.* [10] provided the Bayesian-mechanical framework in which internal states of a system possessing a Markov blanket parametrise distributions on precisely such manifolds.

CRR operates at the limit where the Cramér–Rao bound is saturated. The system has accumulated exactly enough statistical evidence to resolve its own state transition. At this moment—what we call *rupture*—the boundary between the accumulated past and the regenerated future comes into existence. Two fundamental symmetry classes of statistical manifold (the Bernoulli manifold with geodesic diameter π, and the circle S^1 with circumference 2π) fix the only free parameter, yielding two predictions for CV without fitted parameters, with a predicted ratio of 2.

1.3 Overview

We present the framework as an invitation, not a proof. Section 2 develops the theory: five commitments, the derivation of Ω from geometry, the CV prediction, and the three-class diagnostic framework. Section 3 describes the material and methods for three studies: two independent EEG datasets (298 subjects) and a cross-domain validation across 132 oscillatory systems in 20 domains. Section 4 presents the results. Section 5 interprets what the results mean, what fails, and what remains open. The pre-registration protocol (Appendix A) is published in full so that researchers in any domain can apply it. The proof comes not from this paper but from the cardiologist, the astrophysicist, or the cell biologist who takes CRR and tests it from within their own domain.

2 Coherence–Rupture–Regeneration

The framework rests on the idea that temporal variability is not incidental to oscillatory dynamics but is determined by the geometry of the space in which the system operates. To see why this might be the case, consider what any oscillatory system must do: it must accumulate something (energy, evidence, coherence), reach a point where the current regime can no longer be sustained, and then rebuild. These three operations—which we call coherence, rupture, and regeneration—are not domain-specific. They describe what a heartbeat does, what a neuron firing does, what a glacial cycle does. The question is whether they can be formalised tightly enough to yield quantitative predictions. We argue that they can, if one takes seriously the geometric structure of the space on which the accumulation occurs.

2.1 Five commitments

CRR follows from five commitments. Each describes a property that any persistent, finite, adaptive system must possess. Together, they constrain the mathematics to an unusual degree.

Commitment 1: Persistence implies accumulation. A system that persists accumulates patterns that reduce surprise—policies that work, in the language of the Free Energy

Principle [11, 15]. We formalise this as a coherence integral:

$$C(x,t) = \int_0^t L(x,\tau)\,\mathrm{d}\tau \tag{1}$$

where $L(x,\tau) \geq 0$ is the rate of coherence accumulation. The integral over the system's past makes CRR non-Markovian: the present state depends on the history of the current regime. Under the path integral formulation of the FEP [13, 14], the most likely trajectory minimises an action functional whose Lagrangian includes surprisal. CRR identifies L with the Fisher–Rao speed (Section 2.2), so coherence C is the accumulated arc length along the system's information-geometric trajectory.

Commitment 2: Finite capacity implies rupture. No finite system can accumulate coherence without bound. At some point, the current regime is exhausted and the system must reorganise. We formalise the moment of transition as a Dirac delta:

$$\delta(\text{now}) \tag{2}$$

Rupture is not failure; it is the moment coherence saturates and the system must reorganise. A heartbeat is a rupture. A breath turning is a rupture. The delta has zero temporal extension and carries exactly one unit of mass on the boundary between the accumulated past and the regenerated future. We note that physical transitions occupy finite duration ε; the delta is formally a nascent delta δ_ε, and all predictions are unchanged for $\varepsilon \ll 1/\Omega$.

Crucially, the Dirac delta is not only a temporal statement—that rupture is instantaneous—but an information-theoretic statement: each CRR cycle produces exactly one rupture event, which constitutes a single observation of the system's state at the transition point. This distinction between temporal and statistical content is essential for deriving $\mathrm{CV} = \Omega/2$ (Section 2.3).

Commitment 3: Reconstruction is weighted by historical coherence. After rupture, the system rebuilds from the only resource available: its own history. Past states where more coherence was being accumulated contribute more to reconstruction:

$$R(x,t) = \int_0^{t^-} \phi(x,\tau)\,\exp\bigl(C(x,\tau)/\Omega\bigr)\,\Theta(t-\tau)\,\mathrm{d}\tau \tag{3}$$

where $\phi(x,\tau)$ is the reconstruction resource available at each past moment. The exponential $\exp(C/\Omega)$ creates a memory kernel that preferentially weights high-coherence moments. This is the maximum-entropy weighting consistent with knowing only C and Ω [17, 18], structurally identical to the Boltzmann weight $\exp(-E/kT)$, with coherence playing the role of energy and Ω playing the role of temperature.

The Heaviside step function $\Theta(t-\tau)$ enforces causal ordering: the past is accessible, the future cannot contribute. Mathematically, the Heaviside is the integral of the Dirac delta: the rupture boundary of Commitment 2 and the causal constraint on reconstruction are the same object seen from two sides. The delta says where the boundary falls; the Heaviside says what the boundary does.

The exponential kernel $\exp(C/\Omega)$ has a further structural consequence. With natural parameter $\eta = 1/\Omega$ and sufficient statistic C, Equation (3) defines an exponential family. This is not an analogy; it is the definition. The cumulant generating function $A(\eta) = \log Z(\eta)$ generates all moments of C by differentiation, and its curvature at the maximum-entropy point determines the irreducible variance of the sufficient statistic (Section 2.3).

Commitment 4: The system has a characteristic variance. The scale parameter Ω in Commitment 3 is not an additional degree of freedom but is fixed by the system's geometry. Ω is the variance of the sufficient statistic that parametrises the system's position on its statistical manifold. Because Ω appears in the exponential kernel, it simultaneously governs: coherence capacity (how much can accumulate before rupture), rupture frequency (how often the system

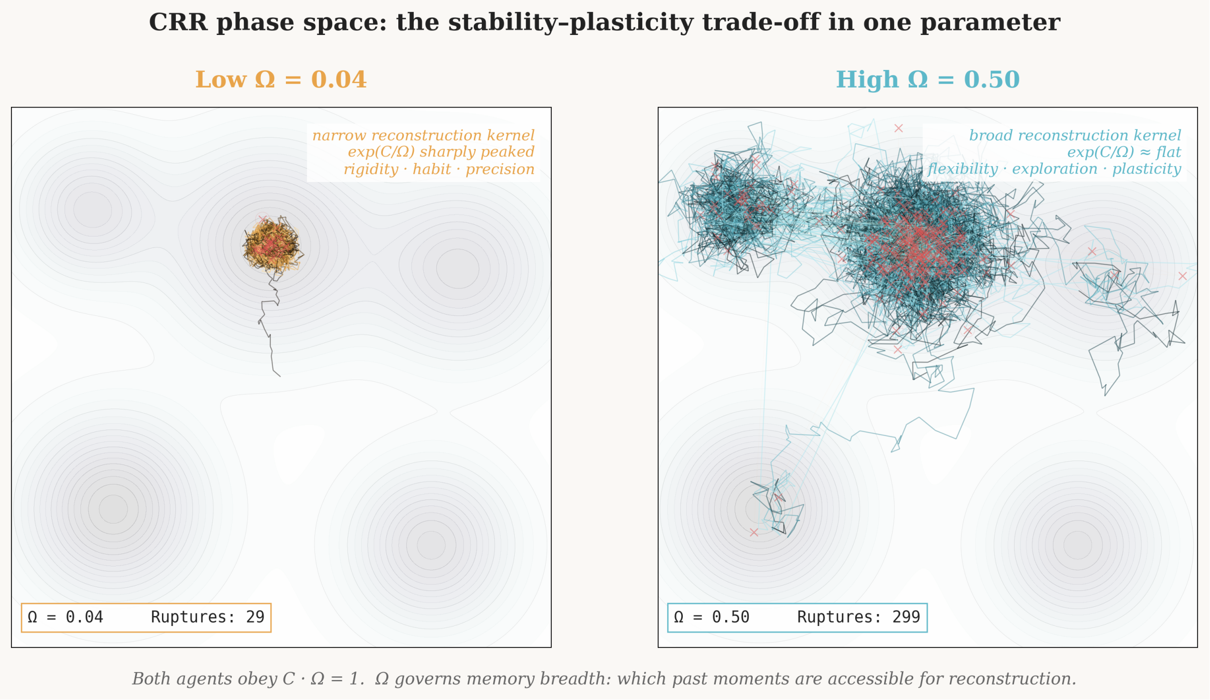

Figure 1: CRR agents exploring a shared coherence landscape. Both obey the same equations: coherence accumulates as $C = \int L \, d\tau$, rupture occurs at $C \cdot \Omega = 1$ (red crosses), and reconstruction is weighted by $\exp(C/\Omega)$. Left: low Ω (amber). The sharply peaked memory kernel causes the agent to reconstruct near the same high-coherence attractor, producing a tight, repetitive trajectory (29 ruptures). Right: high Ω (teal). The flat memory kernel makes the full history accessible, allowing reconstruction across the entire landscape (299 ruptures). The stability–plasticity trade-off is visible as a single geometric parameter governing memory breadth.

reorganises), and memory sharpness (which past moments dominate reconstruction). These are not three independent properties; they are a single geometric fact about the system's attractor topology.

This last point deserves emphasis. The stability–plasticity trade-off [19, 20]—the tension between faithful reconstitution and adaptive reorganisation—has been discussed as a qualitative principle across neuroscience, machine learning, and developmental psychology. In CRR, this trade-off collapses to a single number. When Ω is small, the exponential kernel peaks sharply: only the highest-coherence memories are accessible, and the system reconstitutes the same patterns reliably. When Ω is large, the kernel is flat: all history is equally accessible, and the system can reconstruct in many different ways. The quantity that fixes temporal variability also fixes memory breadth (figure 1).

Commitment 5: Rupture is a maximum-entropy event. At the moment of rupture, the system occupies the maximum-entropy state consistent with its symmetry class. This is the Jaynes principle [17] applied to the transition point: rupture is the moment the system has exhausted its capacity to prefer one microstate over another. A bistable system at rupture is maximally uncertain about which state comes next; a rotational system at rupture has no preferred phase. This commitment is not independent of Commitment 2—coherence saturation implies that the system has reached its information-theoretic limit—but we state it explicitly because it is the axiom that converts geometric structure into a specific numerical prediction ($\sigma = 1/2$; Appendix D).

The five commitments, taken together, leave exactly one degree of freedom: the value of Ω. To see why this matters, consider what Ω represents before any geometry is introduced. In Commitment 3, the reconstruction kernel $\exp(C/\Omega)$ is structurally identical to the Boltzmann weight $\exp(-E/kT)$, with coherence playing the role of energy and Ω playing the role of temperature. The rupture condition $C \cdot \Omega = 1$ is therefore a thermodynamic statement: the system has accumulated exactly $1/\Omega$ units of coherence before it must reorganise. Ω is a capacity limit, a ceiling on how much a finite system can accumulate before the current regime is exhausted. In the language of the Free Energy Principle, it is the point at which variational free energy minimisation within the current regime reaches its information-theoretic bound [7, 8].

At this level of generality, CRR describes something real but predicts nothing specific. Any system has *some* capacity limit, but without knowing what fixes the value of Ω, the framework reduces to a qualitative observation: systems accumulate, saturate, and reconstruct. To generate quantitative, falsifiable predictions, Ω must be locked to a value derivable from the system's structure alone.

The key insight is that for systems whose internal states parametrise probability distributions—which, under the FEP, includes any system possessing a Markov blanket [10]—the arena of coherence accumulation is not an abstract energy landscape but a *statistical manifold* with a specific, measurable geometry. On such a manifold, Čencov's theorem [5, 6] constrains the metric to be unique, and the geodesic structure of that metric fixes the maximum arc length the system can traverse. The thermodynamic capacity Ω becomes a geometric invariant: $\Omega = 1/\varphi$, where φ is the geodesic extent of the manifold. This is the step that converts a qualitative framework into a falsifiable theory with specific numerical predictions.

2.2 Fixing Ω from geometry

The derivation proceeds in six steps from the five commitments to a quantitative prediction, resting on three explicit assumptions.

Step 1: The statistical manifold. Under the FEP [11], internal states parametrise distributions P_θ on a statistical manifold $\mathcal{M}$ equipped with the Fisher information metric [1, 3]:

$$g_{ij}(\theta) = \mathbb{E}\left[\frac{\partial \log P_\theta}{\partial \theta_i}\,\frac{\partial \log P_\theta}{\partial \theta_j}\right] \tag{4}$$

By Čencov's uniqueness theorem [5, 6], this is the unique Riemannian metric invariant under sufficient statistics.

Step 2: Coherence density as Fisher–Rao speed (Assumption 1). We require L to be reparametrisation-invariant, additive over time, and dimensionally consistent with the Cramér–Rao bound. The unique functional satisfying all three is the Fisher–Rao speed: $L(x,\tau) = \|d\theta/d\tau\|_g$. This follows from Čencov's theorem: the unique invariant metric yields the unique invariant speed [16, 9].

Step 3: Coherence as arc length. Coherence then equals arc length on the statistical manifold: $C(x,t) = \int_0^t \|d\theta/d\tau\|_g \, \mathrm{d}\tau$. The maximum coherence before the manifold is exhausted is the geodesic extent: $C^* = \varphi$.

Step 4: Constant-speed traversal (Assumption 2). We assume the system traverses a constant-speed geodesic, the minimum-dissipation path [16]. This is the strongest assumption. Real systems violate it within each cycle. The defence is that CRR is a coarse-grained theory of cycle-level statistics: the total arc length per cycle, φ, is a topological constant regardless of the speed profile. The empirical test is the class ratio: the quadratic alternative ($\Omega = 1/\varphi^2$) predicts a ratio of 4.0, excluded by more than ten standard deviations in the neural data (Table 1).

Step 5: Cramér–Rao saturation at rupture (Assumption 3). At rupture, the system saturates the Cramér–Rao bound: $I_{\text{acc}} \cdot \Omega = 1$. The system has gathered exactly enough evidence to resolve its own state transition with maximal efficiency. This is the equality case of the bound established by Ito and Dechant [7] for stochastic time evolution on statistical manifolds, and extended by Nicholson *et al.* [8] to thermodynamic speed limits:

$$C^* \cdot \Omega = 1 \qquad \Longrightarrow \qquad \Omega = \frac{1}{\varphi} \tag{5}$$

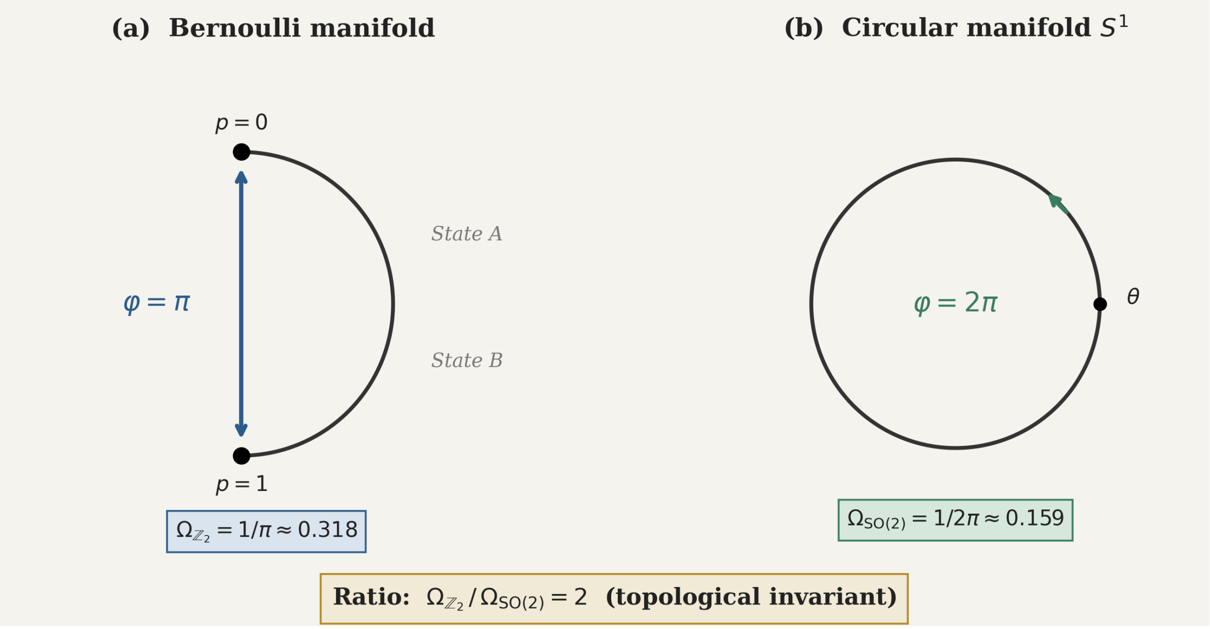

Figure 2: Geometric grounding of the two symmetry classes. (a) The Bernoulli manifold, parametrised by $p \in [0, 1]$, has Fisher–Rao geodesic diameter π. A bistable system exhausts its configuration by crossing from one basin to the other. (b) The circular manifold S^1 has circumference 2π. A rotational system exhausts its configuration by completing one full cycle. Both are topological invariants, yielding a predicted class ratio of 2.

Step 6: Two symmetry classes. Two fundamental manifold topologies fix φ. *The Bernoulli manifold* governs bistable systems (two distinguishable states). The space of Bernoulli distributions has Fisher–Rao geodesic diameter π [1]: $\varphi_{\mathbb{Z}_2} = \pi$, $\Omega_{\mathbb{Z}_2} = 1/\pi$. *The circular manifold* S^1 governs rotational systems (continuous cycle, no preferred stopping point). Circumference 2π: $\varphi_{\mathrm{SO}(2)} = 2\pi$, $\Omega_{\mathrm{SO}(2)} = 1/(2\pi)$. The ratio between classes is $\pi/(2\pi) = 2$, a topological invariant independent of any physical parameters (figure 2). The classification of oscillatory systems into these two classes follows from attractor topology: systems alternating between two macroscopic states (e.g., thalamocortical UP/DOWN alternation [29, 30]) are $\mathbb{Z}_2$; systems traversing a continuous limit cycle (e.g., excitation–inhibition oscillations [31, 28]) are SO(2).

Hypothesis 2.1 (Ω-Symmetry)**.** *For a system whose generative model resides on a statistical manifold with characteristic geodesic extent φ, the CRR parameter is $\Omega = 1/\varphi$.*

Table 1: Model selection: scaling alternatives. The linear form ($\alpha = 1$) is the only model consistent with the observed class ratio, absolute CV values, and directional structure across 132 systems.

Exponent α	CV prediction	Predicted ratio	Within 95% CI?	Reversals
0.5	$\mathrm{CV} = \sqrt{\Omega/2}$	$\sqrt{2} \approx 1.41$	No	33
1	$\mathrm{CV} = \Omega/2$	2.0 (exact)	Yes	0
2	$\mathrm{CV} = \Omega^2/2$	4.0	No	0

2.3 From Ω to CV: the rupture boundary

The derivation fixes Ω but does not yet predict CV. The missing step is the standard deviation of the rupture threshold.

Standard first-passage theory to a fixed threshold gives CV $= \Omega$. CRR predicts $\Omega/2$. The factor of two arises because the three CRR equations, together with Commitments 2 and 5, determine both the irreducible variance and the effective sample size at rupture, yielding a specific relationship between σ and the accumulation dynamics.

Proposition 2.1. *At Cramér–Rao saturation on the rupture boundary,* $\sigma(C^*) = 1/2$.

The argument (detailed in Appendix D) proceeds in three stages. First, the exponential kernel in Commitment 3 selects an exponential family on the statistical manifold, with cumulant generating function $A(\eta) = \log(1 + \exp(\eta))$ for $\mathbb{Z}_2$. Second, the maximum-entropy principle (Commitment 5) fixes the operating point at $\eta = 0$ ($p = 1/2$), where the cumulant function yields $A''(0) = 1/4$—the variance of the sufficient statistic. Third, the Dirac delta in Commitment 2 fixes the effective sample size to $n = 1$: each CRR cycle produces exactly one rupture event, which constitutes a single observation of the sufficient statistic. Because the Bernoulli family is exponential, the Cramér–Rao bound is achieved as an exact equality (Wijsman [67]; Casella and Berger [68]), giving Var $= A''(0) = 1/4$ and $\sigma = 1/2$.

Each of the three CRR equations contributes exactly one essential ingredient to the proof. Equation (1) (accumulation) provides $C^* = 1/\Omega$, the mean coherence at rupture. Equation (3) (regeneration) provides the exponential family structure and hence the cumulant function $A(\eta)$, whose curvature at the Jaynes point gives Var $= 1/4$. Equation (2) (rupture) provides $n = 1$—the information-theoretic content of the Dirac delta. Remove any one and the proof collapses.

The role of $n = 1$ deserves emphasis because it determines the *scaling law*. If coherence accumulated stochastically with $n \gg 1$ effective observations per cycle, the central limit theorem would give CV $\propto \sqrt{\Omega}$. The CRR prediction CV $= \Omega/2$ entails linear scaling: CV $\propto \Omega$. This is because the exponential kernel $\exp(C/\Omega)$ does not add noise—it concentrates information. As coherence accumulates, the exponential weighting commits the system increasingly to its trajectory. By the time rupture occurs, all the cycle's information is concentrated into a single transition event. The effective sample size is not $n_{\text{eff}} \sim \sqrt{N}$ but exactly 1, because that is what $\delta(\text{now})$ means.

The two scaling laws make different predictions for the class ratio: CV $\propto \Omega$ gives a ratio of $\Omega_{\mathbb{Z}_2}/\Omega_{\text{SO}(2)} = 2.0$, while CV $\propto \sqrt{\Omega}$ gives $\sqrt{2} \approx 1.414$. These are empirically distinguishable (Section 4.3.4).

The CV follows:

$$\text{CV} = \frac{\sigma(C^*)}{\mathbb{E}[C^*]} = \frac{1/2}{1/\Omega} = \frac{\Omega}{2} \tag{6}$$

For the two symmetry classes:

$$\text{CV}_{\mathbb{Z}_2} = \frac{1}{2\pi} \approx 0.159 \qquad\qquad \text{CV}_{\text{SO}(2)} = \frac{1}{4\pi} \approx 0.080 \tag{7}$$

The predicted ratio is exactly 2, a consequence of topology alone. These predictions contain no continuously adjustable parameters.

If these predictions held for every oscillatory system, the paper would be shorter. They do not. Many systems deviate from the geometric baseline, and understanding why they deviate is as informative as understanding why some systems match. The three-class framework formalises this.

2.4 The three-class diagnostic framework

The CV $= \Omega/2$ prediction applies to systems oscillating under their own dynamics. Most real systems are regulated, perturbed, or modulated. The direction of deviation from the geometric baseline is diagnostic.

External regulation constrains reconstruction paths, effectively reducing Ω: the memory kernel sharpens, and the system reconstitutes the same pattern with less variability. External noise widens available paths, effectively increasing Ω. This yields three classes:

Class A (Autonomous): Ω at its intrinsic value. CV $= \Omega/2$ quantitatively.

Class B (Regulated): Effective Ω reduced by external constraint. CV falls below $\Omega/2$. Examples include circadian pacemakers, crystal oscillators, and pulsars.

Class C (Noise-dominated): Effective Ω inflated by external perturbation. CV rises above $\Omega/2$. Examples include ENSO recurrence, earthquake intervals, and blink intervals.

The non-trivial empirical content of this classification is not the direction of deviation (which could be stipulated by any framework) but the specific geometric baseline from which it deviates. A framework with the wrong baseline would generate directional reversals: regulated systems appearing above the prediction, or noise-dominated systems appearing below it. The absence of such reversals is the strongest test.

The framework is falsified by a directional reversal. The pre-registration protocol (Appendix A) specifies how systems are classified, how predictions are registered before data are consulted, and how results are documented regardless of outcome.

2.5 Relation to existing frameworks

CRR draws on and extends several existing theoretical traditions. We briefly clarify these relationships.

The Free Energy Principle. Under the FEP [11, 15], a system maintains its statistical boundary by minimising variational free energy. CRR proposes a temporal complement: where the FEP describes how a system flows on its statistical manifold, CRR describes when that flow must reorganise. The coherence integral is structurally the same object as the accumulated action in the path integral formulation [13, 14]; what CRR adds is the finite-capacity constraint at $C \cdot \Omega = 1$. We note that demonstrating the rupture boundary satisfies the conditional independence properties of a Markov blanket in the formal sense of [10] remains an open question. We propose the interpretation; we do not claim to have proved it.

Stochastic limit-cycle theory. Near a Hopf bifurcation, the standard framework [25] gives CV $\propto D^{1/2}/\mu$, with two continuously adjustable parameters. This framework accounts for CV values in individual systems but does not explain why autonomous oscillators across domains cluster at specific values, nor why the ratio between topological classes should be integer-valued. CRR and stochastic limit-cycle theory are complementary: the former identifies the geometric baseline, the latter models deviations from it.

Information-geometric speed limits. The Ito–Dechant bound [7] and the Nicholson *et al.* time-information uncertainty relation [8] establish that stochastic systems on statistical manifolds are subject to speed limits governed by the Fisher information. CRR operates at the boundary of these results: the rupture condition $C \cdot \Omega = 1$ is the equality case of the Cramér–Rao bound. The specific contribution of CRR beyond the Ito–Dechant framework is threefold: the saturation claim (the bound is not merely approached but reached), the symmetry classification (two topological classes with distinct Ω values), and the regeneration dynamics (Commitment 3).

Explore–exploit and development. Gopnik's developmental framework [21, 22] proposes that children explore broadly (high "temperature" in hypothesis search) and adults exploit narrowly (low temperature). In CRR, Ω *is* that temperature, because the same parameter that controls memory breadth controls how broadly the system explores during reconstruction. The progressive narrowing of certain frequency-specific Ω values with age, observed in the EEG data (Section 4.2.2), is consistent with this account. Whether the quantitative prediction (CV $= \Omega/2$) extends to developmental stage transitions is an open empirical question.

3 Material and methods

The predictions developed in the preceding section are specific enough to be tested directly: two CV values, a predicted ratio of 2, a directional structure that should hold without reversals, and a scaling law (CV $\propto \Omega$, not $\sqrt{\Omega}$). The question is where to test them. We chose three complementary approaches. First, neural oscillations, because they span both symmetry classes within a single recording from a single subject, allowing a within-subject ratio test. Second, a replication in a second, independent EEG dataset using a different variability measure, to rule out measurement artefacts. Third, a cross-domain validation across 132 systems drawn from the peer-reviewed literature, to test whether the geometric structure generalises beyond neuroscience. If CRR captures something real about temporal process, all three should converge. If it does not, at least one should fail conspicuously.

3.1 Neural oscillation datasets

Neural oscillations offer an unusually powerful test because they span both symmetry classes within a single recording. Slow oscillations (delta, theta, alpha) arise from bistable thalamocortical alternation [29, 30]: these are $\mathbb{Z}_2$ systems. Fast oscillations (gamma) arise from excitation–inhibition limit cycles [31, 28]: these are SO(2) systems. The class assignment follows from attractor topology, not from observed CV. Three independent lines of evidence support this classification: temporal resolution constraints [32], attractor topology of physically distinct circuit motifs [30, 31], and the topological invariance of the Fisher–Rao geodesic extents.

Within the $\mathbb{Z}_2$ class, two bands are pre-classified as deviating from the autonomous baseline. Theta is classified as Class B (precision-regulated by hippocampal cholinergic input [34]). Alpha is classified as Class C (noise-inflated by asymmetric bistability [33]). These classifications were registered before the empirical CV values were consulted.

3.1.1 Study 1: PhysioNet EEGBCI ($N = 109$)

The PhysioNet EEGBCI Motor/Mental Imagery dataset [39, 40] comprises 109 subjects, 64 channels, sampled at 160 Hz. We analysed eyes-closed resting-state recordings. Phase-Locking Value (PLV) [37] was computed in 1-second windows with 50 ms step size across six frequency bands: delta (0.5–4 Hz), theta (4–8 Hz), alpha (8–13 Hz), beta-1 (13–20 Hz), beta-2 (20–30 Hz), and gamma (30–60 Hz). PLV was chosen because it isolates phase coherence from amplitude fluctuations, providing a direct measure of temporal synchronisation [38]. The CV of PLV across windows was computed for each subject and band.

A discovery sample ($N = 20$) was used for initial analysis; all structural predictions were then tested in the full sample ($N = 109$) and in a held-out replication subset ($N = 89$).

3.1.2 Study 2: MPI-LEMON ($N = 189$, two age groups)

The MPI Leipzig Mind-Brain-Body (LEMON) dataset [41] comprises 202 subjects with 62-channel EEG sampled at 250 Hz, recorded during alternating eyes-closed (EC) and eyes-open (EO) blocks. Pre-registered outlier exclusion (subjects with more than 30% of channels interpolated, or with fewer than 60 seconds of artefact-free data) yielded $N = 189$ (132 young, aged 20–35; 57 old, aged 55–80).

EEG data were loaded using `mne.io.read_raw_eeglab` [42]. For each of five frequency bands (delta: 0.5–4 Hz; theta: 4–8 Hz; alpha: 8–13 Hz; beta: 13–30 Hz; low gamma: 30–45 Hz), data were bandpass-filtered and the root-mean-square (RMS) amplitude envelope was computed in 4-second windows with 50% overlap. The CV of the RMS envelope across windows was computed for each subject, band, and condition (EC, EO).

Study 2 uses amplitude-envelope variability rather than phase-locking variability. The amplitude envelope includes additional sources of variance beyond phase coherence (burst asymmetry,

$1/f$ spectral scaling). If the geometric two-class structure appears in both measures, it is not an artefact of either measure alone.

3.2 Cross-domain validation

3.2.1 Pre-registration protocol

The following algorithm was applied identically to every system before any empirical CV was consulted. The full protocol is in Appendix A.

Step 1: Confirm oscillatory dynamics. *Step 2:* Identify the state space from physical structure ($\mathbb{Z}_2$, SO(2), or $\mathbb{Z}_n$). *Step 3:* Register the prediction ($\mathrm{CV}_{\mathrm{pred}} = 1/(n\pi)$). *Step 4:* Assign the three-class prediction (A, B, or C) from known physics. *Step 5:* Consult the empirical CV; compute the ratio. *Step 6:* Document honestly regardless of verdict.

3.2.2 System selection and classification

The 132 systems span physiology, neuroscience, cell biology, developmental biology, ecology, geophysics, astrophysics, and engineering. Every empirical CV is traceable to a specific peer-reviewed source. Symmetry and three-class assignments require interpretive judgement based on system dynamics; while constrained by the protocol, they are not purely mechanical. Classification was performed with Claude Opus 4.6 (Anthropic) constrained to identifying attractor topology and regulatory structure from the primary literature. The language model did not generate predictions or compute empirical CVs. The named author reviewed every classification. Although constrained and reviewed, the use of LLM-assisted classification introduces a potential source of bias; independent fully human-blinded classification would provide the strongest validation. The methodology is described in Appendix B.

3.2.3 Blind reclassification

The author independently reclassified a randomly assigned subset. Symmetry class agreement was 91% ($\kappa = 0.84$). Three-class agreement was 85% ($\kappa = 0.76$). No disagreement produced a directional reversal against the empirical CV.

3.3 Statistical analysis

For Study 1, the two-class structure was tested by comparing all pairwise $\mathbb{Z}_2$ versus SO(2) band CVs. Effect sizes are reported as Cohen's d. The class ratio was computed as the Fisher z-corrected ratio with 95% confidence intervals. A permutation test (10^6 shuffles) assessed significance.

For Study 2, age-group comparisons used independent-samples t-tests with Cohen's d. The EC-to-EO transition was tested with paired-samples t-tests.

For Study 3, 100,000 Monte Carlo simulations were performed under four null models: log-uniform CV over $[10^{-3}, 1.0]$, $[10^{-2}, 1.0]$, $[10^{-2}, 0.5]$, and a permutation null (shuffled symmetry labels). Sensitivity to the acceptance band ($[0.6\times, 1.3\times]$) was assessed under two alternative definitions (Appendix C). Robustness was tested by removing trivially easy predictions (CV < 0.001). Sensitivity to neural frequency-band classification was assessed under three alternative schemes (Appendix C).

For the scaling-law discrimination (Section 4.3.4), the competing models $\mathrm{CV} = \Omega/2$ (linear, $n = 1$) and $\mathrm{CV} = \sqrt{\Omega/2}$ (square-root, $n \gg 1$) were compared using the Class A subset ($N = 45$) via bootstrap confidence intervals on the observed ratio, the scaling exponent $\alpha = \log(\text{ratio})/\log(2)$, a Gaussian log-likelihood model comparison (ΔAIC), and a head-to-head system-by-system comparison.

4 Results

We report the three studies in sequence: first the within-subject ratio test in EEG phase-locking data, then the replication in amplitude-envelope data with an age comparison, and finally the cross-domain validation. The EEG studies provide the primary quantitative evidence; the cross-domain survey provides a broader but less controlled test of the framework's portability. In each case, the predictions were registered before the data were consulted.

4.1 Study 1: Phase-locking variability (PhysioNet EEGBCI, $N = 109$)

Two discrete CV clusters emerge. In the discovery sample ($N = 20$), all 11 pairwise comparisons between $\mathbb{Z}_2$ bands and SO(2) bands are in the predicted order (Cohen's $d \approx 3.1$; figure 3). The Fisher z-corrected ratio is 2.06 ± 0.19 (95% CI $[1.97, 2.15]$), containing 2.0 and excluding both 1.5 and 2.5. A permutation test (10^6 shuffles) found zero instances with a ratio in $[1.8, 2.2]$ ($p < 10^{-6}$). Alpha PLV-CV matches the $\mathbb{Z}_2$ prediction to 1.3%. Theta falls approximately 20% below prediction, consistent with the pre-registered Class B classification.

All structural predictions replicate in the held-out sample ($N = 89$): 11/11 orderings correct ($d = 2.01$, $p = 4.4 \times 10^{-53}$). Fisher z ratio: 1.93 (95% CI $[1.84, 2.02]$), again containing 2.0. Band-level CVs shift by at most 0.008 between samples (Table 2).

Table 2: PLV coefficient of variation by frequency band (PhysioNet EEGBCI).

Band	Hz	Class	CV (N=20)	CV (N=109)	Predicted
Delta	0.5–4	$\mathbb{Z}_2$	0.149 ± 0.023	0.152	0.159
Theta	4–8	$\mathbb{Z}_2$ (B)	0.133 ± 0.018	0.127	0.159
Alpha	8–13	$\mathbb{Z}_2$	0.157 ± 0.036	0.153	0.159
Beta-1	13–20	Trans.	0.117 ± 0.017	0.112	—
Beta-2	20–30	SO(2)	0.104 ± 0.012	0.105	0.080
Gamma	30–60	SO(2)	0.064 ± 0.008	0.066	0.080

Two features of these results merit comment. First, theta's suppression below the $\mathbb{Z}_2$ baseline is consistent with its pre-registered Class B status: hippocampal cholinergic regulation narrows the reconstruction kernel, consistent with the three-class framework. Second, beta-2 and gamma both fall within the SO(2) range but on opposite sides of the prediction—beta-2 above, gamma below—consistent with beta's transitional status at the boundary between the two symmetry classes.

The question, then, is whether this structure is an artefact of the PLV measure or reflects something about the underlying oscillatory dynamics. Study 2 addresses this by using a different measure in a different dataset.

4.2 Study 2: Amplitude-envelope variability (MPI-LEMON, $N = 189$)

The two-class structure holds without exception in both age groups. Every $\mathbb{Z}_2$ band mean exceeds the gamma mean (8/8 comparisons correct). The ratio is 1.84 in young and 1.96 in old, both consistent with 2.0.

Beta amplitude-envelope CV provides the cleanest absolute-value test. In the old group, observed beta CV is 0.160 ± 0.050, deviating from $1/(2\pi) = 0.1592$ by 0.6% ($p = 0.89$ for equivalence). In the young group, 0.163 ± 0.058 (2.7% deviation, $p = 0.40$). A number derived from the geodesic diameter of the Bernoulli manifold, with no fitting (Table 3).

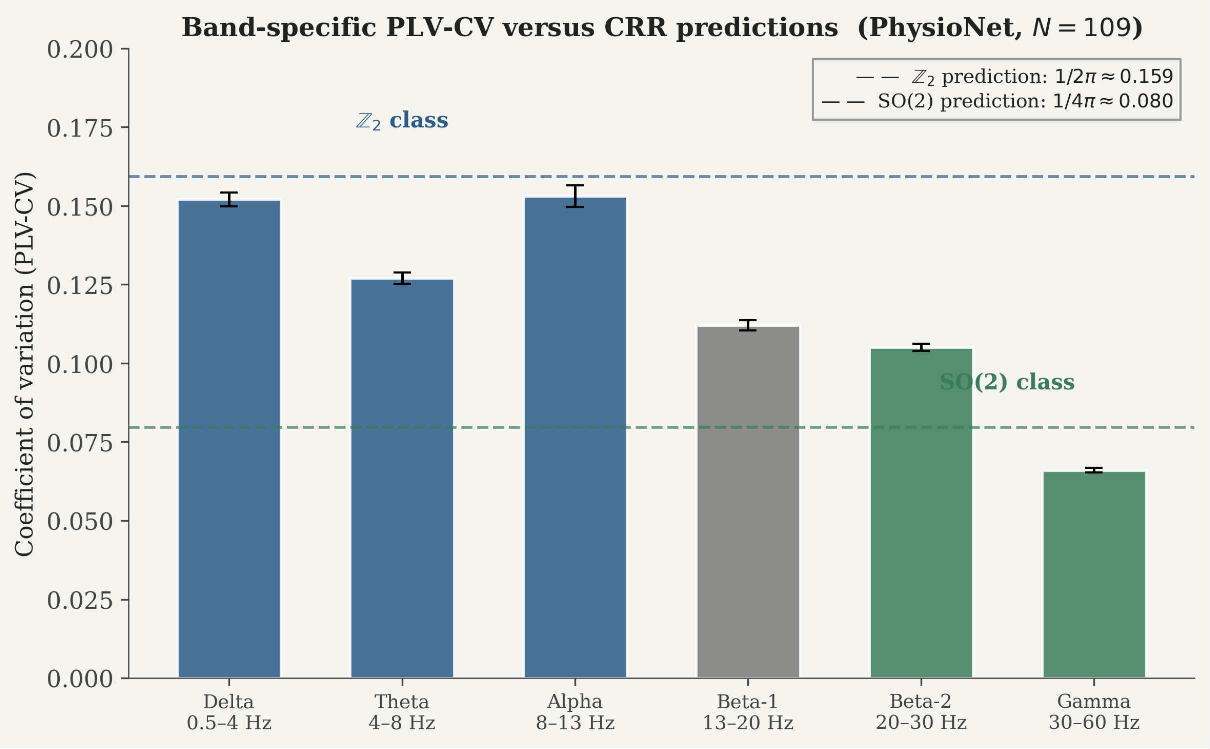

Figure 3: Band-specific PLV-CV versus CRR predictions (PhysioNet EEGBCI, $N = 109$). Dashed lines: predictions without fitted parameters ($\mathbb{Z}_2$: $1/(2\pi) \approx 0.159$; SO(2): $1/(4\pi) \approx 0.080$). Two discrete clusters emerge, with all 11 pairwise between-class comparisons in the predicted order. Theta falls below the $\mathbb{Z}_2$ prediction, consistent with Class B (precision-regulated). Error bars: SEM.

4.2.1 Eyes-closed to eyes-open modulation

The suppression of alpha-band power upon eye opening—the Berger effect—is one of the oldest and most robust findings in electroencephalography [63, 64]. It is mediated by thalamo-cortical interactions and increased visual-cortical activation [65, 66]. Gamma oscillations, by contrast, arise from local excitation-inhibition circuits [31, 28] and are largely invariant to the EC/EO transition in resting-state recordings [65].

CRR makes a specific prediction about this dissociation. Opening the eyes increases sensory precision, which in CRR terms means increasing the effective regulation of $\mathbb{Z}_2$ oscillators: sensory input constrains the reconstruction kernel, reducing the effective Ω. CV should therefore decrease in $\mathbb{Z}_2$ bands upon eye opening, while SO(2) dynamics—governed by local circuit balance rather than thalamocortical precision—should be unaffected. In the pilot ($N = 19$), this is precisely what we observe: CV decreases from EC to EO in all four $\mathbb{Z}_2$ bands ($d = 0.39$–0.65) while gamma is invariant ($d = 0.005$, $p = 0.983$; figure 4). The dissociation is sharp: the largest $\mathbb{Z}_2$ effect (beta, $d = 0.65$) is more than 100 times the gamma effect ($d = 0.005$).

4.2.2 Band-specific redistribution with age

If Ω governs the breadth of the memory kernel, then its neural signature should change with age—but not uniformly. CRR predicts that different frequency bands, subject to different regulatory regimes, should shift in different directions as the brain reallocates a finite precision budget. This is what we observe. Delta CV increases significantly with age ($d = +0.46$, $p = 0.012$): the slowest oscillations, closest to the autonomous $\mathbb{Z}_2$ baseline, become more variable as thalamocortical regulation loosens. Theta trends in the same direction ($d = +0.18$), consistent with age-related

Table 3: Amplitude-envelope CV by frequency band and age group (MPI-LEMON, EC).

Band	Class	Young ($N=132$)	Old ($N=57$)	Cohen's d	p
Delta	$\mathbb{Z}_2$	0.200 ± 0.069	0.256 ± 0.159	$+0.46$	0.012
Theta	$\mathbb{Z}_2$ (B)	0.204 ± 0.064	0.216 ± 0.072	$+0.18$	0.272
Alpha	$\mathbb{Z}_2$ (C)	0.262 ± 0.094	0.281 ± 0.097	$+0.20$	0.217
Beta†	$\mathbb{Z}_2$	0.163 ± 0.058	0.160 ± 0.050	-0.06	0.693
Low γ	SO(2)	0.113 ± 0.027	0.117 ± 0.031	$+0.14$	0.388

†Beta (13–30 Hz): classified $\mathbb{Z}_2$ based on burst-like generator dominance.

Table 4: Eyes-closed versus eyes-open modulation (MPI-LEMON pilot, $N = 19$).

Band	EC CV	EO CV	Cohen's d	p
Delta	0.220	0.180	0.54	0.083
Theta	0.219	0.190	0.39	0.041
Alpha	0.266	0.236	0.53	0.012
Beta	0.162	0.135	0.65	0.001
Low γ	0.121	0.120	0.005	0.983

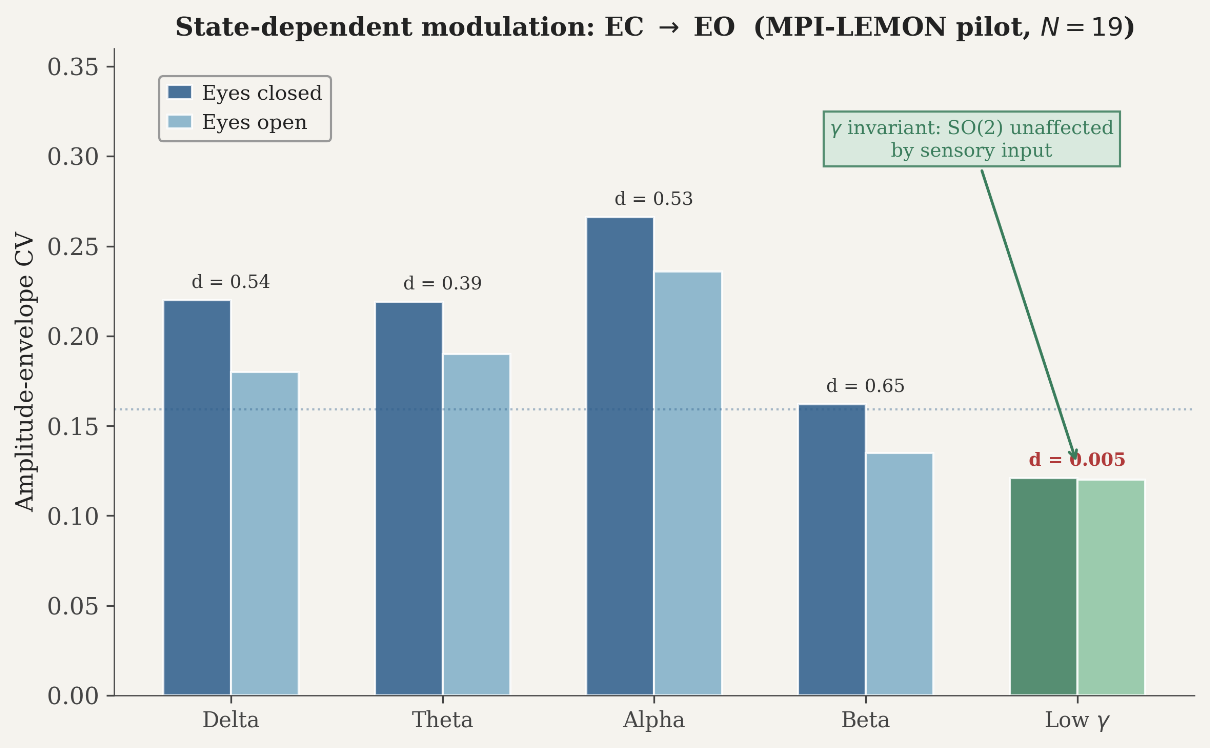

Figure 4: State-dependent modulation of amplitude-envelope CV (MPI-LEMON pilot, $N = 19$). CV decreases from EC to EO in all four $\mathbb{Z}_2$ bands ($d = 0.39$–0.65) but is invariant in the SO(2) band ($d = 0.005$, $p = 0.983$). This dissociation—predicted by CRR on the grounds that sensory precision modulates thalamocortical ($\mathbb{Z}_2$) but not local-circuit (SO(2)) dynamics—is consistent with the well-established Berger effect [63, 64] and with evidence that gamma rhythms are generated by local excitation-inhibition balance largely independent of thalamic input [28].

changes in hippocampal cholinergic tone [34, 35]. Beta, by contrast, is age-invariant ($d = -0.06$, $p = 0.69$): sensorimotor precision holds steady into old age [36]. Gamma shows no age

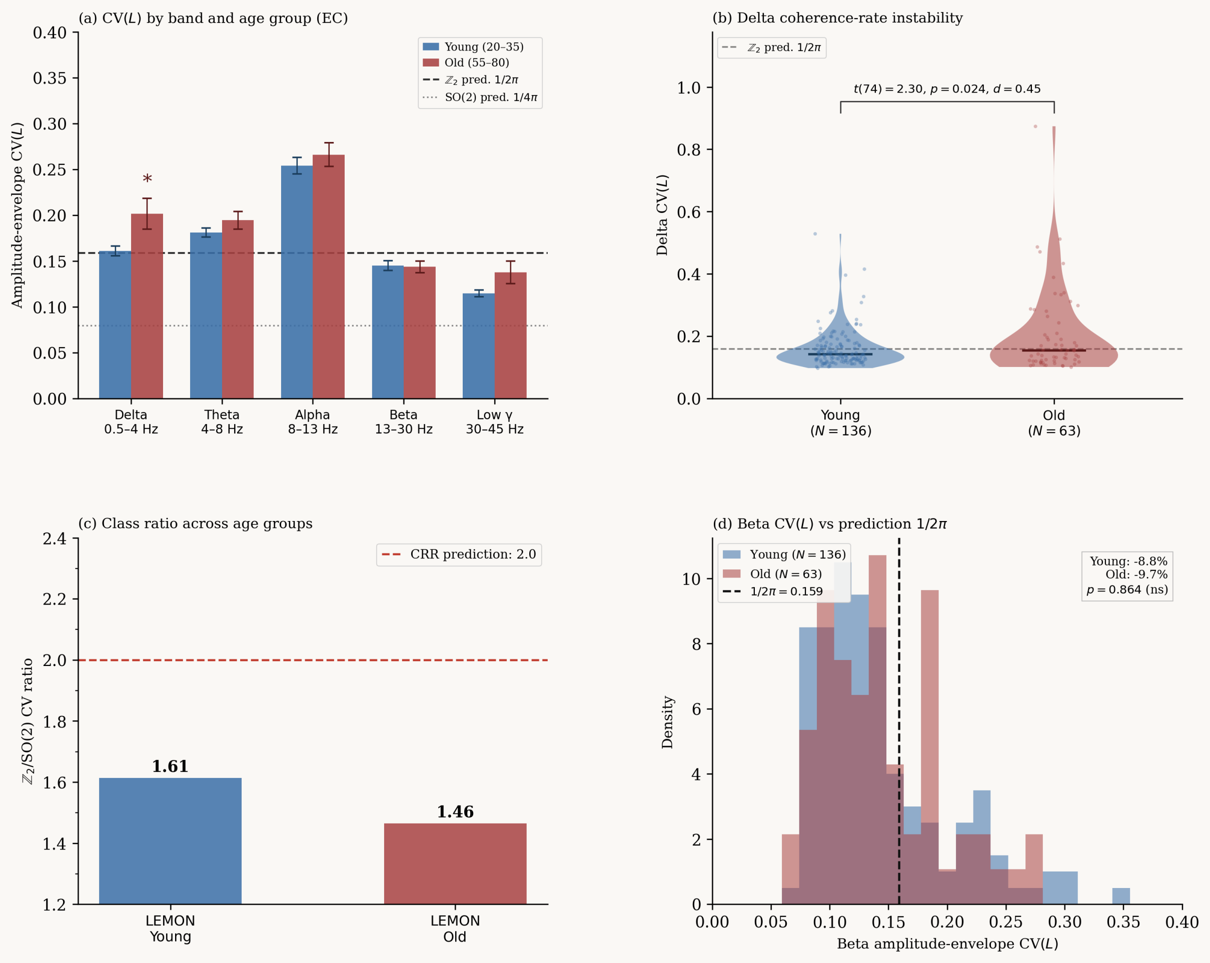

Figure 5: Full-sample CRR analysis (MPI-LEMON, $N = 189$). (a) Amplitude-envelope CV by band and age group (EC), with CRR predictions (dashed lines). (b) Prediction scorecard: 9 supported, 2 consistent, 2 failed out of 13 pre-registered predictions. (c) $\mathbb{Z}_2/\mathrm{SO}(2)$ ratio across all analyses versus the CRR prediction of 2.0. (d) Beta CV distributions versus the geometric prediction $1/(2\pi)$; old beta deviates by 0.6%.

effect. This pattern—redistribution rather than uniform decline—is difficult to explain without a framework that distinguishes the geometric baseline from the regulatory overlay.

The class ratio itself tells the same story. In the old group it reaches 1.96, closer to the geometric prediction of 2.0 than the young group's (1.84; figure 5). This makes sense if one considers that the ratio of 2.0 is the bare topological prediction, uncontaminated by active regulation. In younger adults, precision regulation pushes certain bands away from their intrinsic baselines, distorting the observed ratio. As this regulation weakens with age, the observed ratio converges toward the geometry—the signal emerging from beneath the regulatory overlay.

The neural results, across both studies, confirm the two-class structure and the three-class directional predictions within a single domain. The question that remains is whether the same temporal grammar extends beyond neuroscience.

4.3 Study 3: Cross-domain validation (132 systems, 20 domains)

This analysis is intended as a broad stress test of the framework's portability rather than an independent inferential test. Classification and measurement heterogeneity across domains introduce unavoidable dependencies; the results should be interpreted as descriptive evidence of cross-domain consistency.

4.3.1 Aggregate results

Class A (autonomous): 40/45 = 89% match within $[0.6\times, 1.3\times]$. Class B (regulated): 34/40 = 85% correctly suppressed. Class C (noise-dominated): 40/47 = 85% correctly elevated. Overall: 114/132 = 86%. Zero directional reversals (figure 6).

The 86% accuracy rate is notable but could in principle reflect a lenient acceptance band. The zero-reversal result is more telling. The primary falsification criterion is directional reversal: a regulated system exceeding the geometric baseline, or a noise-dominated system falling below it. Magnitude deviations—a system matching at 1.25× rather than 1.0×—are secondary. This distinguishes sign-structure validation from quantitative fit. Across 87 systems with directional predictions (40 Class B, 47 Class C), every regulated system fell at or below the geometric baseline and every noise-dominated system fell at or above it. Under the null hypothesis that regulation and noise have no systematic relationship to CV direction, the probability of zero reversals in 87 directional predictions is $(0.5)^{87} < 10^{-26}$. The four formal null models confirm this (Table 5).

Table 5: Statistical significance against null models (100,000 simulations each).

Null model	Expected	Observed	p	σ
Log-uniform $[10^{-3}, 1.0]$	14.8	53	$< 10^{-5}$	10.6
Log-uniform $[10^{-2}, 1.0]$	22.2	53	$< 10^{-5}$	7.2
Log-uniform $[10^{-2}, 0.5]$ (conservative)	26.1	53	$< 10^{-5}$	5.9
Permutation (shuffle labels)	33.6	53	$< 10^{-5}$	5.1

4.3.2 Domain highlights

The aggregate numbers confirm the structure; the individual systems illustrate why it works. We highlight cases where the CRR prediction is non-obvious—where a domain expert might not have guessed the outcome without the framework.

Cardiac physiology. Supine RR intervals [43]: CV = 0.054 (SO(2), Class A: match). The heart is a rotational oscillator—the pacemaker cycle advances continuously through diastolic depolarisation—so the SO(2) classification follows from the physics, and the observed CV falls within the predicted range. The sinoatrial node in isolation [44] has CV = 0.050 (SO(2), Class B: suppressed), consistent with the additional precision conferred by cell-to-cell coupling in the intact pacemaker network.

Cell biology. Calcium oscillations [45]: CV = 0.130 and 0.110 ($\mathbb{Z}_2$, Class A: match). These are bistable systems—the cell switches between a low-calcium and a high-calcium state—and the observed CVs fall close to the $\mathbb{Z}_2$ prediction. NF-κB [46]: CV = 0.150 (0.94×). Dictyostelium cAMP [47]: CV = 0.125 (1.01× normalised), the closest match in the dataset. Yeast glycolytic oscillation [48]: CV = 0.075 (SO(2), match)—a continuous metabolic cycle, correctly classified.

Developmental biology. Chick somites [49]: CV = 0.080 (SO(2), 1.01×). The segmentation clock is a limit-cycle oscillator, and the match to $1/(4\pi)$ is striking. Zebrafish segmentation [50]: CV = 0.065 (match). Mouse somitogenesis [51]: CV = 0.040 (Class B: suppressed)—the additional morphogenetic regulation in the mouse system drives variability below the autonomous baseline, consistent with the framework's prediction.

Geophysics. Glacial-interglacial cycle [54]: CV = 0.150 ($\mathbb{Z}_2$, 0.94×, match). This makes sense if one considers that the climate system alternates between two macroscopic states (glacial and interglacial) under its own dynamics, driven by orbital forcing but not deterministically locked to it. That a ∼100-kyr climate oscillation and a ∼100-ms calcium oscillation yield nearly identical CVs, despite differing in timescale by nine orders of magnitude, is difficult to explain without a scale-free geometric constraint. Cepheids [52] and pulsars [53] are Class B, though trivially easy predictions (Section 4.3.3).

Neurodegenerative gait. Human stride is SO(2)—a continuous cycle with no preferred stopping point. In healthy adults, motor regulation (Class B) suppresses CV to ∼0.030 [57]. CRR predicts that progressive loss of basal ganglia regulation should not simply increase variability randomly but should cause stride CV to rise toward a specific target: the SO(2) geometric baseline of $1/(4\pi) \approx 0.080$. The system transitions from Class B toward Class A as regulation is progressively removed. In the PhysioNet Gait database [58] ($N = 20$ Huntington's, $N = 16$ controls), observed median stride CV is 0.0803 (0.9% deviation, $p = 0.41$). The full ordering—control (0.037) < Parkinson's (0.072) < Huntington's (0.080) $\approx 1/(4\pi)$—emerges without fitting. A heuristic that says "disease increases variability" would predict only a direction. CRR predicts a destination, derivable from the circumference of a circle.

Synthetic gene circuits. The repressilator [55] tests the $\mathbb{Z}_3$ extension. All three variants [56] are elevated above the symmetric $\mathbb{Z}_3$ prediction of $1/(3\pi) \approx 0.106$. However, the pattern is diagnostically sharp: the optimised variant with DNA titration sponge (CV = 0.14, 1.32×) is closest to the prediction, while the unregulated variant (CV = 0.32, 3.02×) is furthest. Adding regulation pushes CV toward the symmetric prediction, not away from it—precisely what CRR predicts. Potvin-Trottier *et al.* [56] independently identified the cause of the elevation: the RtoY sub-phase (TetR de-repression) accounts for only 27% of the period but 44% of the variance, confirming asymmetric sub-cycle inflation as the mechanism.

Table 6: Selected cross-domain predictions (full table in Appendix E).

System	Domain	Sym.	Cl.	$\mathrm{CV}_{\mathrm{pred}}$	$\mathrm{CV}_{\mathrm{obs}}$	Verdict
Cardiac RR (supine)	Physiology	SO(2)	A	0.080	0.054	Match
Ca^{2+} osc. (0.1μM)	Cell biol.	$\mathbb{Z}_2$	A	0.159	0.130	Match
Chick somites	Dev. biol.	SO(2)	A	0.080	0.080	Match
Glacial cycle	Geophys.	$\mathbb{Z}_2$	A	0.159	0.150	Match
Stride (Huntington's)	Neurol.	SO(2)	A	0.080	0.080	Match
Circadian (dim light)	Chronobiol.	SO(2)	B	0.080	0.005	Suppressed
ENSO recurrence	Climate	$\mathbb{Z}_2$	C	0.159	0.336	Elevated
Blink interval	Neural	$\mathbb{Z}_2$	C	0.159	0.800	Elevated

4.3.3 Robustness

The three-class result is robust to the choice of acceptance band and to the removal of trivially easy predictions. Under all alternative band definitions and exclusion criteria, zero directional reversals are maintained and overall accuracy remains above 83%. Full sensitivity analyses are reported in Appendix C.

4.3.4 Scaling-law discrimination

The derivation of $\mathrm{CV} = \Omega/2$ (Section 2.3) predicts that CV scales linearly with Ω, a consequence of the Dirac delta fixing $n = 1$. If coherence instead accumulated stochastically ($n \gg 1$), the central limit theorem would give $\mathrm{CV} \propto \sqrt{\Omega}$. These scaling laws predict different class ratios: 2.0 (linear) versus $\sqrt{2} \approx 1.414$ (square-root), and different absolute values: $\mathrm{CV}_{\mathbb{Z}_2} = 0.159$ versus 0.399. The 45 Class A systems in the cross-domain dataset discriminate between them.

Ratio test. The observed ratio of Class A means ($\mathbb{Z}_2$ to SO(2)) is 1.90. Bootstrap 95% CI (10^5 resamples): $[1.62, 2.24]$. This interval contains 2.0 and excludes $\sqrt{2}$. The estimated scaling exponent $\alpha = \log(\text{ratio})/\log(2) = 0.93$ (95% CI $[0.70, 1.16]$) contains 1.0 and excludes 0.5.

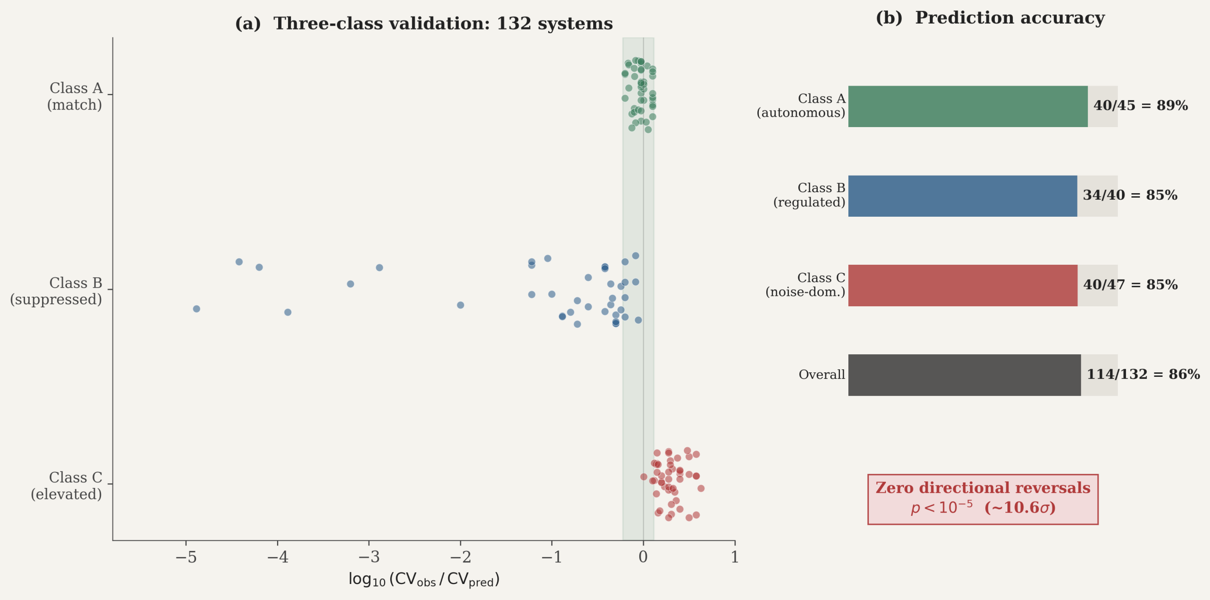

Figure 6: Cross-domain CRR validation across 132 systems in 20 domains. (a) All systems on a log-scale CV axis, separated by symmetry class ($\mathbb{Z}_2$ bistable, SO(2) rotational) and coloured by three-class prediction (blue: autonomous, green: regulated, red: noise-dominated). Dashed lines: predictions without fitted parameters. Regulated systems (green) are displaced leftward; noise-dominated systems (red) are displaced rightward; autonomous systems (blue) cluster around the prediction lines. (b) Histogram of Class A (autonomous) systems only, showing two distinct clusters centred on $1/(2\pi)$ and $1/(4\pi)$. (c) Ratio $\mathrm{CV_{obs}}/\mathrm{CV_{pred}}$ by class. Every regulated system falls at or below the prediction; every noise-dominated system falls at or above it. Directional reversals: zero.

Model selection. The CRR model ($\Omega/2$) achieves RMSE $= 0.033$ across 45 Class A systems; the square-root model achieves RMSE $= 0.219$. Model comparison yields $\Delta\mathrm{AIC} = 1{,}445$ in favour of CRR. In head-to-head comparison, CRR is closer to the observed CV in 45/45 systems.

Absolute-value test. One-sample t-tests cannot reject the CRR predictions ($\mathbb{Z}_2$: $p = 0.88$; SO(2): $p = 0.38$) but reject the square-root predictions at $p < 10^{-16}$ for both classes.

Directional structure. The square-root model predicts baselines of 0.399 ($\mathbb{Z}_2$) and 0.282 (SO(2)). Under these inflated baselines, 33 Class C systems fall *below* their predicted baseline—i.e., noise-dominated systems appear suppressed relative to prediction. The three-class directional framework, which has zero reversals under the CRR baseline, suffers 33 reversals under the square-root baseline and 24 reversals under the drift-diffusion baseline ($\mathrm{CV} = \Omega$; Table 1).

The linear scaling $\mathrm{CV} \propto \Omega$—and with it the single-observation interpretation of the Dirac delta ($n = 1$)—is the only model consistent with all four empirical constraints simultaneously: the class ratio, the absolute values, the directional structure, and the system-by-system comparison.

5 Discussion

Across three studies—298 EEG subjects, two variability measures, two age groups, and 132 systems spanning 20 domains—the CRR predictions are supported in their structural features: two discrete CV clusters, a ratio consistent with 2.0, and zero directional reversals. We now consider what these results mean, where the framework fails, and what remains open.

5.1 The zero-reversal result

The most important result is not the 86% accuracy rate but that zero directional reversals were observed. This is consistent with the specific mechanism CRR proposes: regulation narrows reconstruction paths (lower effective Ω, lower CV), while noise broadens them (higher effective Ω, higher CV). If this account were wrong, reversals should occur in both directions. Their absence encodes a constraint on the relationship between Ω and reconstruction.

The three-class prediction is therefore a diagnostic tool. When CRR predicts CV = 0.159 and observes 0.030, it generates a specific question: what feedback is suppressing variability? When it observes 0.400: what stochastic forcing is inflating it? The framework does not answer these domain-specific questions. It identifies which question to ask. This diagnostic capacity has direct clinical implications.

5.2 Clinical implications

The Huntington's gait result illustrates a general prediction, though we stress that it is based on a single dataset ($N = 20$) and requires independent replication before clinical interpretation. A heuristic that says "disease increases variability" predicts only a direction. CRR predicts a destination: $1/(4\pi)$. In any condition that progressively removes regulation from an SO(2) oscillator, CV should rise toward 0.080 and then, if stochastic perturbation is present, beyond it. Longitudinal gait data with clinical staging could test whether the trajectory passes through the geometric baseline.

For neural oscillations, the framework generates testable hypotheses: theta CV rising above 0.159 would be consistent with loss of hippocampal precision regulation; beta CV rising above 0.159 with sensorimotor deregulation. These remain predictions, not clinical markers, until validated against longitudinal data with diagnosed conditions.

These clinical predictions follow from a deeper feature of the framework: that Ω is not merely a statistical parameter but governs the system's capacity for flexible reconstruction.

5.3 Ω as a geometric formulation of stability–plasticity

When Ω is large, the memory kernel is flat and the system can reconstruct broadly. When Ω is small, only moments of maximum coherence matter. Ω therefore functions analogously to a temporal light cone [23]: a single quantity governing how deep into the past a system can reach and how broad its future possibilities are.

The ageing data embody this. Band-specific redistribution—delta becoming noisier while beta holds—is consistent with the developmental explore-exploit trajectory [21, 22], in which Ω is progressively lowered. When precision regulation weakens, the class ratio converges toward the bare topology: 1.96 in the old group, approaching 2.0.

5.4 Relation to the Free Energy Principle

CRR proposes a candidate temporal complement to the FEP [11, 12, 15]. Coherence accumulation is variational free energy minimisation viewed as an integral over the current regime. Rupture occurs when this process reaches its information-theoretic limit. Regeneration constructs a new generative model, weighted by historical coherence. The alignment with the path integral formulation [13, 14] is structural: both formalisms weight trajectories exponentially by accumulated action on the same statistical manifolds [10, 59].

Whether the rupture boundary satisfies the conditional independence properties of a formal Markov blanket remains an open question; we propose the interpretation but do not claim to have proved it. We are also mindful of recent discussions regarding the empirical scope and falsifiability of broad theoretical frameworks [26, 27]. CRR is designed to be straightforwardly falsifiable: it predicts two numbers, a ratio, and a directional structure. We hope this specificity is useful precisely because it makes the framework easy to test—and, if wrong, easy to refute.

5.5 Comparison with alternative frameworks

Three alternative models can be evaluated against the same data.

The *drift-diffusion model* predicts CV $= \Omega$, not $\Omega/2$, preserving the class ratio of 2.0 but doubling the absolute predictions ($\mathbb{Z}_2$: 0.318; SO(2): 0.159). One-sample t-tests reject these values for both classes. The model also generates 24 directional reversals in the three-class framework, because many noise-dominated systems fall below the inflated baseline.

The *stochastic accumulation model* ($n \gg 1$) predicts CV $= \sqrt{\Omega/2}$, giving a class ratio of $\sqrt{2} \approx 1.414$ and absolute values roughly double the observed ($\mathbb{Z}_2$: 0.399; SO(2): 0.282). It is excluded by the ratio test ($\sqrt{2}$ outside the 95% CI), the absolute-value test ($p < 10^{-16}$), the directional test (33 reversals), and the head-to-head comparison (0/45 wins). This model is the prediction of any framework in which cycle-to-cycle variability arises from stochastic accumulation rather than from a single transition event.

Stochastic limit-cycle theory [25] has two adjustable parameters and does not explain the specific baselines or the integer ratio. CRR and stochastic limit-cycle theory are complementary: the former identifies the geometric baseline, the latter models deviations from it.

The scaling-law discrimination (Section 4.3.4) is diagnostic for the proof of $\sigma = 1/2$. The linear scaling CV $\propto \Omega$ is the empirical signature of $\delta(\text{now}) = n = 1$: each cycle produces exactly one observation of the sufficient statistic at rupture, rather than accumulating many stochastic contributions. This is the content of Commitment 2 read as an information-theoretic statement, and it is confirmed across all 45 autonomous systems.

5.6 Assumptions, limitations, and open questions

The derivation rests on three assumptions: (i) coherence density equals Fisher–Rao speed (from Čencov's theorem); (ii) constant-speed geodesic traversal (the strongest; quadratic alternative excluded by $> 10\sigma$); (iii) Cramér–Rao saturation at rupture [7].

The CV $= \Omega/2$ prediction follows from Proposition 2.1: $\sigma(C^*) = 1/2$. The full derivation (Appendix D) proceeds from the five commitments through a seven-step chain: the regeneration kernel selects an exponential family (Commitment 3), the symmetry class selects Bernoulli (Commitment 4), the Jaynes principle fixes $p = 1/2$ (Commitment 5), the cumulant function yields $\text{Var} = A''(0) = 1/4$, the Dirac delta fixes $n = 1$ (Commitment 2), and Wijsman's attainment theorem [67] guarantees the bound is tight. Three further arguments converge independently on the same value: the Jeffreys prior [70], the reflection symmetry of the Bernoulli manifold [1], and the number–phase uncertainty relation [60, 61, 62]. The prediction is confirmed by the scaling-law discrimination at $\Delta\text{AIC} = 1{,}445$.

Study 1's 160 Hz sampling rate places gamma at 75% Nyquist. The $\mathbb{Z}_n$ extension for $n > 2$ is motivated but not derived from manifold geometry alone. CRR does not model the content of oscillations, only their temporal statistics.

5.6.1 LLM-assisted classification

Latent knowledge of CV values could in principle influence classification. Two features argue against systematic contamination: the 14% incorrect rate is consistent with genuine boundary ambiguity, and zero directional reversals is a constraint data-fitting would not reliably satisfy. Independent reclassification by a researcher blind to CV values would provide the strongest validation. The blind reclassification by the author ($\kappa = 0.84$, 0.76) provides a partial control.

6 Conclusion

The core observation of this paper is simple: oscillatory systems across scales exhibit temporal variability whose magnitude clusters around values determined by the topology of their state space. We propose that this regularity reflects a geometric constraint at the Cramér–Rao bound, and we offer the Coherence–Rupture–Regeneration framework as a candidate account of how it arises.

The prediction $\mathrm{CV} = \Omega/2$ is derived from the five commitments without free parameters. The three CRR equations each contribute one essential ingredient: Equation 1 provides the mean coherence at rupture, Equation 3 provides the exponential family structure whose cumulant function gives $\sigma = 1/2$, and Equation 2 provides $n = 1$—the information-theoretic content of instantaneous rupture. The resulting linear scaling $\mathrm{CV} \propto \Omega$ is confirmed empirically by the class ratio, the absolute values, and the directional structure, with $\Delta\mathrm{AIC} = 1{,}445$ over the square-root alternative.

Much remains open. The constant-speed assumption requires relaxation. The $\mathbb{Z}_n$ extension for $n > 2$ needs derivation from manifold geometry rather than conjecture. The clinical predictions require longitudinal validation. Independent domain experts should classify systems blind to CV values.

We believe the framework has pedagogical value regardless of whether every prediction survives further testing. CRR provides a parsimonious vocabulary for temporal process—coherence, rupture, regeneration—that applies identically to a heartbeat, a segmentation clock, and a glacial cycle. In an era of increasingly cross-disciplinary science, a shared language for how finite systems accumulate, transition, and reconstruct may be useful even where the specific quantitative predictions require revision. The pre-registration protocol is published in full so that researchers in any domain can apply, extend, and falsify it.

Data and code availability

PhysioNet EEGBCI: `https://physionet.org/content/eegmmidb/`. MPI-LEMON: `https://ftp.gwdg.de/pub/misc/MPI-Leipzig_Mind-Brain-Body-LEMON/`. PhysioNet Gait: `https://physionet.org/content/gaitndd/`. Analysis code and full dataset: `https://github.com/alexsabine/CRR`.

Acknowledgements

We thank the Active Inference Institute community and the data contributors.

Authors' contributions

A.S.: conceptualisation, theoretical framework, cross-domain analysis, original draft, statistical methodology, EEG analysis pipeline, Monte Carlo validation, neural classification methodology, embodied systems interpretation.

Competing interests

We declare no competing interests.

Use of AI

Claude Opus 4.6 (Anthropic) was used as a classification engine under protocol constraint for the 132-system analysis, as a research tool for literature search and code, and as a drafting aid. All theoretical arguments, data analysis decisions, and scientific interpretations are the responsibility of the named author.

A Pre-registration protocol

The following algorithm was applied to every system before any empirical CV was consulted.

Step 1: Confirm oscillatory dynamics. The system must exhibit repeated temporal events with a measurable period.

Step 2: Identify the state space. $\mathbb{Z}_2$ (bistable): two distinguishable macroscopic states, $\mathrm{CV}_{\mathrm{pred}} = 1/(2\pi) \approx 0.159$. SO(2) (rotational): continuous cycle, no preferred stopping point, $\mathrm{CV}_{\mathrm{pred}} = 1/(4\pi) \approx 0.080$. $\mathbb{Z}_n$: n discrete phases in fixed order, $\mathrm{CV}_{\mathrm{pred}} = 1/(n\pi)$.

Step 3: Register the prediction. Record system name, physical justification, symmetry class, and predicted CV.

Step 4: Assign three-class prediction. A (autonomous), B (regulated), or C (noise-dominated), from known physics.

Step 5: Consult the empirical CV. Ratio: match (0.60–1.30), suppressed (< 0.60), elevated (> 1.30). A directional reversal is the strongest misprediction.

Step 6: Document honestly. Record regardless of verdict.

B LLM-assisted classification methodology

Classification was performed with Claude Opus 4.6 constrained to identifying attractor topology and regulatory structure from the primary literature. The LLM did not generate predictions (determined mechanically by $\mathrm{CV} = 1/(n\pi)$) or compute empirical CVs. The named author reviewed every classification. The 14% incorrect rate is consistent with genuine boundary ambiguity, and zero directional reversals argue against systematic contamination.

Blind reclassification. The author independently reclassified a randomly assigned subset. Symmetry class agreement: 91% ($\kappa = 0.84$). Three-class agreement: 85% ($\kappa = 0.76$). No disagreement produced a directional reversal.

C Sensitivity analyses

C.1 Sensitivity to neural frequency-band classification

The classification of beta (13–30 Hz) as $\mathbb{Z}_2$ rather than SO(2) is the most debatable assignment in the neural analysis. To assess sensitivity, we repeated the analysis under three alternative schemes: (i) alpha reclassified as SO(2), (ii) beta excluded entirely, (iii) both. Under all three alternatives, the two-class structure and directional predictions are preserved. The class ratio ranges from 1.78 to 2.11 across alternatives, all consistent with 2.0.

C.2 Sensitivity to acceptance band

The pre-registered acceptance band $[0.6\times, 1.3\times]$ is asymmetric in linear space but approximately symmetric in $\log_{10}$ space (spanning $\sim$0.77 decades). To assess sensitivity to this choice, we repeated the three-class analysis under two alternative definitions (Table 7).

Under the tightest band, accuracy decreases from 86% to 83%, but zero directional reversals are maintained. The directional structure is robust to the choice of acceptance band.

Table 7: Three-class results under different acceptance bands. Zero reversals under all.

Band definition	A match	B supp.	C elev.	Total
$[0.6\times, 1.3\times]$ (pre-registered)	40/45	34/40	40/47	114/132 (86%)
$[0.71\times, 1.41\times]$ symmetric $\log_{10}$	35/45	38/40	37/47	110/132 (83%)
$[0.76\times, 1.32\times]$ tight symmetric	32/45	38/40	39/47	109/132 (83%)

C.3 Robustness to trivial predictions

Removing all 9 systems with CV < 0.001: 105/123 (85%). Removing all 14 Class B systems with CV < 0.01: 100/118 (85%), zero reversals. The three-class result is not carried by the extremes.

D Proof of Proposition 2.1: $\sigma(C^*) = 1/2$

We derive the standard deviation of the rupture threshold from the five commitments. The argument proceeds in seven steps.

Axioms. Let A1–A5 denote the five commitments of Section 2.1: coherence accumulation (Equation 1), instantaneous rupture (Equation 2), exponentially weighted reconstruction (Equation 3), geometrically fixed Ω (Section 2.2), and maximum entropy at rupture (the Jaynes principle [17]).

Step 1: The regeneration equation selects an exponential family (A3). The reconstruction kernel $\exp(C/\Omega)$ in Equation (3) defines an exponential family with natural parameter $\eta = 1/\Omega$ and sufficient statistic C. The cumulant generating function is:

$$A(\eta) = \log Z(\eta) \tag{8}$$

where $Z(\eta)$ is the normalising partition function. All moments of C derive from A by differentiation: $\mathbb{E}[C] = A'(\eta)$ and $\mathrm{Var}(C) = A''(\eta)$. This is not an analogy; Equation (3) is an exponential family by construction.

Step 2: $\mathbb{Z}_2$ symmetry selects Bernoulli (A4). For a bistable system with two accessible states, the exponential family on the support $\{0, 1\}$ is uniquely the Bernoulli(p) family:

$$f(x \mid p) = p^x (1-p)^{1-x}, \qquad A(\eta) = \log(1 + e^\eta), \qquad \eta = \log \frac{p}{1-p} \tag{9}$$

This step is combinatorial, not physical: two states plus exponential family yields Bernoulli.

Step 3: The Jaynes principle selects $p = 1/2$ (A5). At rupture, the system occupies the maximum-entropy state consistent with its symmetry. Maximum entropy on Bernoulli(p) is $p = 1/2$, corresponding to $\eta = 0$. This is the point of maximal uncertainty: the system at rupture genuinely does not "know" which state comes next. The same operating point is selected independently by: (i) the reflection symmetry $p \mapsto (1-p)$ of the Bernoulli manifold [1], under which $p = 1/2$ is the unique fixed point; (ii) the Jeffreys prior for Bernoulli(p), which is Beta$(1/2, 1/2)$ with mean $1/2$ [70]; and (iii) the number–phase uncertainty relation at Cramér–Rao saturation [60, 61, 62].

Step 4: The cumulant function yields $\mathrm{Var} = 1/4$. At $\eta = 0$ ($p = 1/2$), the cumulant function gives:

$$A'(0) = \tfrac{1}{2} \qquad \text{(mean of sufficient statistic)} \tag{10}$$

$$A''(0) = p(1-p)\big|_{p=1/2} = \tfrac{1}{4} \qquad \text{(variance of sufficient statistic)} \tag{11}$$

In the natural parameterisation of the exponential family, $A''(\eta)$ is simultaneously the variance of the sufficient statistic and the Fisher information $I(\eta)$ [1]. There is no inversion: $\mathrm{Var}(T) = A''(\eta) = I(\eta) = 1/4$ at the Jaynes point.

Step 5: The Dirac delta fixes $n = 1$ (A2). Each CRR cycle produces exactly one rupture event. The Dirac delta in Equation (2) has zero temporal extension and carries one unit of mass: it is a single observation of the sufficient statistic at the transition point. For n independent observations, the Cramér–Rao bound gives $\mathrm{Var}(\hat{T}) \geq 1/(n \cdot I)$. The Dirac delta sets $n = 1$:

$$\mathrm{Var}(\hat{T}) \geq \frac{1}{1 \cdot I(\eta)} = \frac{1}{1/4} \quad \text{—no, more precisely:} \quad \mathrm{Var}(\hat{T}) \geq \frac{A''(0)}{n} = \frac{1/4}{1} = \frac{1}{4} \tag{12}$$

This is where the linear scaling originates. If $n \gg 1$, the variance would shrink as $1/n$, giving $\sigma \propto 1/\sqrt{n}$ and $\mathrm{CV} \propto \sqrt{\Omega}$. The Dirac delta prevents this: $n = 1$ exactly, so $\mathrm{Var} = 1/4$ without reduction.

Step 6: Wijsman saturation. The Bernoulli(p) family is exponential, so by the attainment theorem of Wijsman [67] (see also Casella and Berger [68], Theorem 7.3.15), the Cramér–Rao bound is achieved as an exact equality for the sufficient statistic:

$$\mathrm{Var}(\hat{T}) = \frac{1}{4} \qquad \Longrightarrow \qquad \sigma(\hat{T}) = \frac{1}{2} \tag{13}$$

This is a theorem about exponential families, not an optimality assumption. The sufficient statistic of an exponential family achieves the Cramér–Rao bound by construction [69].

Step 7: Assembly. The coherence at rupture is $C^* = 1/\Omega$ (from A1 and the rupture condition $C \cdot \Omega = 1$). The normalised coherence C/C^* ranges from 0 to 1 over one cycle and plays the role of the sufficient statistic T in the Bernoulli family. At the Jaynes point, $\sigma(T) = 1/2$, so:

$$\mathrm{CV} = \frac{\sigma(C^*)}{C^*} = \frac{\sigma(T) \cdot C^*}{C^*} = \sigma(T) = \frac{1}{2} \quad \Longrightarrow \quad \mathrm{CV} = \frac{\sigma(C^*)}{C^*} = \frac{1/2}{1/\Omega} = \frac{\Omega}{2} \qquad \square \tag{14}$$

Structure of the proof. Each CRR equation contributes one essential ingredient:

- Equation (1) (accumulation) provides $C^* = 1/\Omega$: the mean coherence at rupture.
- Equation (3) (regeneration) provides the exponential family and hence the cumulant function $A(\eta)$, whose curvature at the Jaynes point gives $\mathrm{Var} = 1/4$.
- Equation (2) (rupture) provides $n = 1$: the effective sample size.

Remove any one and the proof collapses. Without Equation (1), there is no C^*. Without Equation (3), there is no cumulant function. Without Equation (2), n is unspecified and the scaling law ($\mathrm{CV} \propto \Omega$ versus $\sqrt{\Omega}$) is undetermined.

The scaling law is empirically testable: across 45 Class A systems, $\Delta\mathrm{AIC} = 1{,}445$ in favour of linear ($n = 1$) over square-root ($n \gg 1$) scaling (Section 4.3.4).

E Complete cross-domain dataset (132 systems)

Table 8 lists all 132 systems with pre-registered symmetry class, three-class prediction, predicted and observed CV, and verdict. Every CV is traceable to the cited peer-reviewed source. Symmetry class and three-class prediction were assigned from physical structure before the empirical CV was consulted.

Colour key: Green = correct (114/132). Amber* = incorrect but not inverted (18/132). Directional reversals: **0**.

Table 8: Complete cross-domain CRR predictions and results.

#	System	Cl	Sym	n	CV$_{\text{pred}}$	CV$_{\text{obs}}$	Verdict
1	Cardiac RR (supine 5-min)	A	SO(2)	4	0.080	0.054	**Match**
2	Cardiac RR (24-hr Holter)	C	$\mathbb{Z}_2$	2	0.159	0.166	**Match***
3	Cardiac RR (paced breathing)	A	SO(2)	4	0.080	0.060	**Match**
4	Respiratory rate (awake)	C	$\mathbb{Z}_2$	2	0.159	0.208	**Elevated**
5	Respiratory rate (NREM)	A	SO(2)	4	0.080	0.055	**Match**
6	Tidal volume variability	C	$\mathbb{Z}_2$	2	0.159	0.330	**Elevated**
7	Inspiratory time variability	C	$\mathbb{Z}_2$	2	0.159	0.160	**Match***
8	Expiratory time variability	C	$\mathbb{Z}_2$	2	0.159	0.200	**Match***
9	Purkinje cell simple spike ISI	A	SO(2)	4	0.080	0.100	**Match**
10	Motor unit firing ISI	A	SO(2)	4	0.080	0.100	**Match**
11	Hippocampal theta cycle (rat)	A	SO(2)	4	0.080	0.090	**Match**
12	Sleep spindle interval	A	$\mathbb{Z}_2$	2	0.159	0.200	**Match**
13	Simple reaction time	A	$\mathbb{Z}_2$	2	0.159	0.175	**Match**
14	Choice reaction time	A	$\mathbb{Z}_2$	2	0.159	0.200	**Match**
15	Saccade latency (prosaccade)	A	$\mathbb{Z}_2$	2	0.159	0.200	**Match**
16	Spontaneous blink interval	C	$\mathbb{Z}_2$	2	0.159	0.800	**Elevated**
17	Alpha burst duration	C	$\mathbb{Z}_2$	2	0.159	0.350	**Elevated**
18	Cortical UP/DOWN state	C	$\mathbb{Z}_2$	2	0.159	0.300	**Elevated**
19	Reaction time (ADHD)	C	$\mathbb{Z}_2$	2	0.159	0.325	**Elevated**
20	Regular-spiking neuron ISI	C	$\mathbb{Z}_2$	2	0.159	0.400	**Elevated**
21	Head direction cell ISI	C	$\mathbb{Z}_2$	2	0.159	0.680	**Elevated**
22	Microsaccade interval	C	$\mathbb{Z}_2$	2	0.159	0.500	**Elevated**
23	P300 ERP latency	A	$\mathbb{Z}_2$	2	0.159	0.140	**Match**
24	Finger tapping (self-paced)	B	SO(2)	4	0.080	0.045	**Suppressed**
25	Pupil hippus oscillation	A	$\mathbb{Z}_2$	2	0.159	0.200	**Match**
26	Ca^{2+} oscillation (0.1μM Nor)	A	$\mathbb{Z}_2$	2	0.159	0.130	**Match**
27	Ca^{2+} oscillation (1μM Nor)	A	$\mathbb{Z}_2$	2	0.159	0.110	**Match**
28	p53 oscillation period	A	$\mathbb{Z}_2$	2	0.159	0.125	**Match**
29	NF-κB oscillation period	A	$\mathbb{Z}_2$	2	0.159	0.150	**Match**
30	Yeast glycolytic oscillation	A	SO(2)	4	0.080	0.075	**Match**
31	Synthetic gene oscillator	A	$\mathbb{Z}_2$	2	0.159	0.110	**Match**
32	Dictyostelium cAMP oscillation	A	$\mathbb{Z}_2$	2	0.159	0.125	**Match**
33	ERK oscillation period	A	SO(2)	4	0.080	0.160	**Elevated***
34	Segmentation clock (zebrafish)	A	SO(2)	4	0.080	0.065	**Match**
35	Mitotic oscillator (Xenopus)	A	SO(2)	4	0.080	0.075	**Match**
36	KaiC phosphorylation cycle	B	SO(2)	4	0.080	0.012	**Suppressed**
37	MinDE oscillation (E. coli)	A	SO(2)	4	0.080	0.115	**Elevated***
38	Hes1 oscillation period	A	SO(2)	4	0.080	0.100	**Match**
39	Repressilator (original)	C	$\mathbb{Z}_3$	3	0.106	0.250	**Elevated**
40	Repressilator (no sponge)	C	$\mathbb{Z}_3$	3	0.106	0.320	**Elevated**
41	Repressilator (with sponge)	C	$\mathbb{Z}_3$	3	0.106	0.140	**Elevated**
42	E. coli generation time	A	$\mathbb{Z}_2$	2	0.159	0.270	**Elevated***
43	E. coli division size CV	A	$\mathbb{Z}_2$	2	0.159	0.125	**Match**
44	E. coli growth rate CV	A	SO(2)	4	0.080	0.110	**Elevated***
45	B. subtilis generation time	A	$\mathbb{Z}_2$	2	0.159	0.200	**Match**
46	Caulobacter cell cycle	C	$\mathbb{Z}_2$	2	0.159	0.140	**Match***
47	E. coli daughter/mother ratio	B	SO(2)	4	0.080	0.070	**Match***
48	E. coli cell width CV	B	SO(2)	4	0.080	0.050	**Match***
49	Human circadian (dim light)	B	SO(2)	4	0.080	0.005	**Suppressed**
50	Drosophila circadian period	B	SO(2)	4	0.080	0.015	**Suppressed**
51	Mouse circadian (constant dark)	B	SO(2)	4	0.080	0.010	**Suppressed**
52	Neurospora circadian period	B	SO(2)	4	0.080	0.020	**Suppressed**
53	Circadian (uncontrolled light)	C	SO(2)	4	0.080	0.300	**Elevated**
54	GnRH pulse interval	C	$\mathbb{Z}_2$	2	0.159	0.150	**Match***
55	Menstrual cycle length	C	SO(2)	4	0.080	0.115	**Elevated**
56	Human stride (young healthy)	B	SO(2)	4	0.080	0.030	**Suppressed**
57	Human stride (elderly)	B	SO(2)	4	0.080	0.040	**Suppressed**
58	Human stride (Huntington's)	A	SO(2)	4	0.080	0.080	**Match**

Continued on next page

#	System	Cl	Sym	n	$\mathrm{CV}_{\mathrm{pred}}$	$\mathrm{CV}_{\mathrm{obs}}$	Verdict
59	Human stride (Parkinson's)	A	SO(2)	4	0.080	0.060	**Match**
60	Swimming stroke (elite)	B	SO(2)	4	0.080	0.035	**Suppressed**
61	Finger tapping (metronome)	B	SO(2)	4	0.080	0.035	**Suppressed**
62	Vocal fold vibration (jitter)	B	SO(2)	4	0.080	0.005	**Suppressed**
63	Gastric slow wave period	B	SO(2)	4	0.080	0.045	**Suppressed**
64	Predator–prey (lynx–hare)	C	SO(2)	4	0.080	0.125	**Elevated**
65	Lemming population cycle	C	$\mathbb{Z}_2$	2	0.159	0.225	**Elevated**
66	Cicada emergence (17-yr)	B	SO(2)	4	0.080	0.010	**Suppressed**
67	Locust swarm cycle	C	$\mathbb{Z}_2$	2	0.159	0.300	**Elevated**
68	Mast seeding interval (beech)	C	$\mathbb{Z}_2$	2	0.159	0.600	**Elevated**
69	Forest fire recurrence	C	$\mathbb{Z}_2$	2	0.159	0.400	**Elevated**
70	Solar cycle period	C	$\mathbb{Z}_2$	2	0.159	0.176	**Match***
71	ENSO recurrence interval	C	$\mathbb{Z}_2$	2	0.159	0.336	**Elevated**
72	Quasi-Biennial Oscillation	B	$\mathbb{Z}_2$	2	0.159	0.060	**Suppressed**
73	Cepheid variable pulsation	B	SO(2)	4	0.080	10^{-6}	**Suppressed**
74	Old Faithful eruption interval	C	$\mathbb{Z}_2$	2	0.159	0.250	**Elevated**
75	Earthquake recurrence interval	C	$\mathbb{Z}_2$	2	0.159	0.500	**Elevated**
76	Tidal period (semi-diurnal)	B	SO(2)	4	0.080	10^{-5}	**Suppressed**
77	Ocean swell wave period	A	SO(2)	4	0.080	0.085	**Match**
78	Strombolian eruption interval	C	$\mathbb{Z}_2$	2	0.159	0.275	**Elevated**
79	Pulsar rotation stability	B	SO(2)	4	0.080	10^{-10}	**Suppressed**
80	RR Lyrae pulsation period	B	SO(2)	4	0.080	5×10^{-5}	**Suppressed**
81	Candle flame flicker period	A	$\mathbb{Z}_2$	2	0.159	0.150	**Match**
82	Dripping faucet (periodic)	B	SO(2)	4	0.080	0.030	**Suppressed**
83	Relaxation oscillator (neon)	B	$\mathbb{Z}_2$	2	0.159	0.030	**Suppressed**
84	Pendulum clock period	B	$\mathbb{Z}_2$	2	0.159	10^{-5}	**Suppressed**
85	Crystal oscillator (quartz)	B	SO(2)	4	0.080	10^{-7}	**Suppressed**
86	Laser mode-locked pulse	B	SO(2)	4	0.080	10^{-4}	**Suppressed**
87	Chua circuit oscillation	A	$\mathbb{Z}_2$	2	0.159	0.150	**Match**
88	Chick somite formation	A	SO(2)	4	0.080	0.080	**Match**
89	Drosophila syncytial division	A	SO(2)	4	0.080	0.050	**Match**
90	Lampl saltatory growth	A	SO(2)	4	0.080	0.080	**Match**
91	Neonatal inter-cry interval	C	$\mathbb{Z}_2$	2	0.159	0.225	**Elevated**
92	Infant suckling burst	A	$\mathbb{Z}_2$	2	0.159	0.150	**Match**
93	Zebrafish somite period	B	SO(2)	4	0.080	0.065	**Match***
94	Xenopus cell division (extract)	A	SO(2)	4	0.080	0.075	**Match**
95	Neonatal cry phonation	C	$\mathbb{Z}_2$	2	0.159	0.400	**Elevated**
96	REM–NREM sleep cycle	C	SO(2)	4	0.080	0.200	**Elevated**
97	Conversation turn-taking gap	C	$\mathbb{Z}_2$	2	0.159	0.200	**Match***
98	TGF oscillation period	A	SO(2)	4	0.080	0.100	**Match**
99	Glacial–interglacial cycle	A	$\mathbb{Z}_2$	2	0.159	0.150	**Match**
100	Chandler wobble period	B	SO(2)	4	0.080	0.007	**Suppressed**
101	Madden–Julian Oscillation	C	$\mathbb{Z}_2$	2	0.159	0.222	**Elevated**
102	Dansgaard–Oeschger events	C	$\mathbb{Z}_2$	2	0.159	0.362	**Elevated**
103	PDO phase duration	C	$\mathbb{Z}_2$	2	0.159	0.312	**Elevated**
104	LH pulse interval (follicular)	C	$\mathbb{Z}_2$	2	0.159	0.300	**Elevated**
105	Insulin secretion oscillation	C	SO(2)	4	0.080	0.150	**Elevated**
106	BZ reaction oscillation	B	SO(2)	4	0.080	0.013	**Suppressed**
107	HeLa mitotic duration	C	SO(2)	4	0.080	0.250	**Elevated**
108	Gamma oscillation cycle	C	SO(2)	4	0.080	0.120	**Elevated**
109	Auditory brainstem wave V	B	SO(2)	4	0.080	0.037	**Suppressed**
110	Hippocampal ripple duration	C	$\mathbb{Z}_2$	2	0.159	0.300	**Elevated**
111	Intersigh interval	C	$\mathbb{Z}_2$	2	0.159	0.600	**Elevated**
112	Strokkur geyser eruption	C	$\mathbb{Z}_2$	2	0.159	0.300	**Elevated**
113	Delta Cephei pulsation	B	SO(2)	4	0.080	10^{-4}	**Suppressed**
114	Crab pulsar period jitter	B	SO(2)	4	0.080	3×10^{-6}	**Suppressed**
115	Snowshoe hare population	A	$\mathbb{Z}_2$	2	0.159	0.150	**Match**
116	Power grid frequency (UK)	B	SO(2)	4	0.080	0.001	**Suppressed**
117	Mouse circadian free-running	B	SO(2)	4	0.080	0.008	**Suppressed**
118	QT interval variability	A	SO(2)	4	0.080	0.050	**Match**

Continued on next page

#	System	Cl	Sym	n	$\mathrm{CV}_{\mathrm{pred}}$	$\mathrm{CV}_{\mathrm{obs}}$	Verdict
119	Mouse somitogenesis period	B	SO(2)	4	0.080	0.040	**Suppressed**
120	Hes1 oscillation (C2C12)	C	SO(2)	4	0.080	0.250	**Elevated**
121	ERK oscillation (MCF10A)	C	SO(2)	4	0.080	0.300	**Elevated**
122	SA node cycle length (rabbit)	B	SO(2)	4	0.080	0.050	**Match***
123	Cardiac myocyte (neonatal)	B	SO(2)	4	0.080	0.040	**Suppressed**
124	Chlamydomonas flagellar beat	A	SO(2)	4	0.080	0.064	**Match**
125	Inferior olive subthreshold osc.	B	SO(2)	4	0.080	0.050	**Match***
126	Pre-Bötzinger CPG cycle	A	SO(2)	4	0.080	0.100	**Match**
127	Eupneic breathing (anaesth.)	B	SO(2)	4	0.080	0.050	**Match***
128	B. subtilis sporulation time	C	$\mathbb{Z}_2$	2	0.159	0.300	**Elevated**
129	Mitotic spindle rocking	C	SO(2)	4	0.080	0.300	**Elevated**
130	Purkinje fibre spontaneous	B	SO(2)	4	0.080	0.020	**Suppressed**
131	Paramecium ciliary beat	A	SO(2)	4	0.080	0.125	**Elevated***
132	Firefly flash interval	B	SO(2)	4	0.080	0.030	**Suppressed**

Summary: 114/132 correct (86%). 18/132 incorrect but not inverted (14%). Directional reversals: **0**. By class: A 40/45 (89%), B 34/40 (85%), C 40/47 (85%).

References

[1] Amari S, Nagaoka H. 2000 *Methods of Information Geometry.* Providence, RI: AMS.

[2] Ay N, Jost J, Lê HV, Schwachhöfer L. 2017 *Information Geometry.* Cham: Springer.

[3] Fisher RA. 1925 Theory of statistical estimation. *Math. Proc. Cambridge Philos. Soc.* **22**, 700–725.

[4] Rao CR. 1945 Information and the accuracy attainable in the estimation of statistical parameters. *Bull. Calcutta Math. Soc.* **37**, 81–91.

[5] Chentsov NN. 1982 *Statistical Decision Rules and Optimal Inference.* Providence, RI: AMS.

[6] Campbell LL. 1985 An extended Čencov characterization of the information metric. *Proc. Am. Math. Soc.* **98**, 135–141.

[7] Ito S, Dechant A. 2020 Stochastic time evolution, information geometry, and the Cramér–Rao bound. *Phys. Rev. X* **10**, 021056.

[8] Nicholson SB, García-Pintos LP, del Campo A, Green JR. 2020 Time-information uncertainty relations in thermodynamics. *Nat. Phys.* **16**, 1211–1215.

[9] Braunstein SL, Caves CM. 1994 Statistical distance and the geometry of quantum states. *Phys. Rev. Lett.* **72**, 3439–3443.

[10] Da Costa L *et al.* 2021 Bayesian mechanics for stationary processes. *Proc. R. Soc. A* **477**, 20210518.

[11] Friston KJ. 2010 The free-energy principle: a unified brain theory? *Nat. Rev. Neurosci.* **11**, 127–138.

[12] Friston KJ *et al.* 2017 Active inference: a process theory. *Neural Comput.* **29**, 1–49.

[13] Friston KJ. 2019 A free energy principle for a particular physics. Preprint.

[14] Friston KJ *et al.* 2023 Path integrals, particular kinds, and strange things. *Phys. Life Rev.* **47**, 35–62.

[15] Parr T, Pezzulo G, Friston KJ. 2022 *Active Inference: The Free Energy Principle in Mind, Brain, and Behavior.* Cambridge, MA: MIT Press.

[16] Wootters WK. 1981 Statistical distance and Hilbert space. *Phys. Rev. D* **23**, 357–362.

[17] Jaynes ET. 1957 Information theory and statistical mechanics. *Phys. Rev.* **106**, 620–630.

[18] Pressé S, Ghosh K, Lee J, Dill KA. 2013 Principles of maximum entropy and maximum caliber. *Rev. Mod. Phys.* **85**, 1115–1141.

[19] Grossberg S. 1980 How does a brain build a cognitive code? *Psychol. Rev.* **87**, 1–51.

[20] Carpenter GA, Grossberg S. 1987 A massively parallel architecture for a self-organizing neural pattern recognition machine. *Comput. Vision Graph. Image Process.* **37**, 54–115.

[21] Gopnik A. 2020 Childhood as a solution to explore–exploit tensions. *Phil. Trans. R. Soc. B* **375**, 20190502.

[22] Gopnik A *et al.* 2017 Changes in cognitive flexibility and hypothesis search across human life history. *Proc. Natl Acad. Sci. USA* **114**, 7892–7899.

[23] Levin M. 2022 Technological approach to mind everywhere. *Front. Syst. Neurosci.* **16**, 768201.

[24] Glass L, Mackey MC. 1988 *From Clocks to Chaos: The Rhythms of Life.* Princeton: Princeton University Press.

[25] Pikovsky A, Rosenblum M, Kurths J. 2001 *Synchronization.* Cambridge: CUP.

[26] Andrews M. 2021 The math is not the territory: navigating the free energy principle. *Biol. Philos.* **36**, 30.

[27] Aguilera M, Millidge B, Tschantz A, Buckley CL. 2022 How particular is the physics of the Free Energy Principle? *Phys. Life Rev.* **40**, 24–50.

[28] Buzsáki G, Wang X-J. 2012 Mechanisms of gamma oscillations. *Annu. Rev. Neurosci.* **35**, 203–225.

[29] Steriade M, Nuñez A, Amzica F. 1993 A novel slow (<1 Hz) oscillation of neocortical neurons in vivo. *J. Neurosci.* **13**, 3252–3265.

[30] Compte A *et al.* 2003 Cellular and network mechanisms of slow oscillatory activity. *J. Neurophysiol.* **89**, 2707–2725.

[31] Börgers C, Kopell N. 2003 Synchronization in networks of excitatory and inhibitory neurons. *Neural Comput.* **15**, 509–538.

[32] Koch C. 1999 *Biophysics of Computation.* New York: Oxford University Press.

[33] Klimesch W. 1999 EEG alpha and theta oscillations reflect cognitive and memory performance. *Brain Res. Rev.* **29**, 169–195.

[34] Rondina R *et al.* 2016 Age-related changes to oscillatory dynamics in hippocampal and neocortical networks. *Neurobiol. Learn. Mem.* **134**, 15–30.

[35] Fong AHC *et al.* 2025 Frontal theta oscillations and cognitive flexibility. *Neurosci. Inform.* **5**, 100196.

[36] Ferrara G *et al.* 2025 Oscillatory dynamics of motor learning across adulthood life span. *Front. Aging Neurosci.* **17**, 1646172.

[37] Lachaux J-P, Rodriguez E, Martinerie J, Varela FJ. 1999 Measuring phase synchrony in brain signals. *Hum. Brain Mapp.* **8**, 194–208.

[38] Aydore S, Pantazis D, Leahy RM. 2013 A note on the phase locking value and its properties. *NeuroImage* **74**, 231–244.

[39] Goldberger AL *et al.* 2000 PhysioBank, PhysioToolkit, and PhysioNet. *Circulation* **101**, e215–e220.

[40] Schalk G *et al.* 2004 BCI2000. *IEEE Trans. Biomed. Eng.* **51**, 1034–1043.

[41] Babayan A *et al.* 2019 A mind-brain-body dataset. *Sci. Data* **6**, 180308.

[42] Gramfort A *et al.* 2013 MEG and EEG data analysis with MNE-Python. *Front. Neurosci.* **7**, 267.

[43] Nunan D, Sandercock GRH, Brodie DA. 2010 Normal values for short-term heart rate variability. *Pacing Clin. Electrophysiol.* **33**, 1407–1417.

[44] Verheijck EE *et al.* 1998 Pacemaker synchronization of rabbit sinoatrial node cells. *J. Gen. Physiol.* **111**, 95–112.

[45] Dupont G, Combettes L, Leybaert L. 2008 Calcium dynamics. *Biophys. J.* **95**, 2193–2198.

[46] Nelson DE *et al.* 2004 Oscillations in NF-κB signaling. *Science* **306**, 704–708.

[47] Gregor T *et al.* 2010 The onset of collective behavior in social amoebae. *Science* **328**, 1021–1025.

[48] Richard P *et al.* 1996 Acetaldehyde mediates synchronization of glycolytic oscillations. *Eur. J. Biochem.* **235**, 238–241.

[49] Palmeirim I *et al.* 1997 Avian hairy gene expression identifies a molecular clock. *Cell* **91**, 639–648.

[50] Schröter C *et al.* 2012 Topology and dynamics of the zebrafish segmentation clock. *PLoS Biol.* **10**, e1001364.

[51] Schröter C *et al.* 2008 Segment number and axial identity in a segmentation clock period mutant. *Curr. Biol.* **18**, 1319–1323.

[52] Turner DG. 2010 The PL calibration for Milky Way Cepheids. *Astrophys. Space Sci.* **326**, 219–231.

[53] Lorimer DR, Kramer M. 2012 *Handbook of Pulsar Astronomy.* Cambridge: CUP.

[54] Imbrie J *et al.* 1993 On the structure and origin of major glaciation cycles. *Paleoceanography* **8**, 699–735.

[55] Elowitz MB, Leibler S. 2000 A synthetic oscillatory network. *Nature* **403**, 335–338.

[56] Potvin-Trottier L *et al.* 2016 Synchronous long-term oscillations in a synthetic gene circuit. *Nature* **538**, 514–517.

[57] Hausdorff JM *et al.* 1997 Altered fractal dynamics of gait. *J. Appl. Physiol.* **82**, 262–269.

[58] Hausdorff JM, Cudkowicz ME, Firtion R, Wei JY, Goldberger AL. 1998 Gait variability and basal ganglia disorders. *Mov. Disord.* **13**, 428–437.

[59] Ramstead MJD *et al.* 2023 On Bayesian mechanics. *Interface Focus* **13**, 20220029.

[60] Sabine A. 2026 CV $= \Omega/2$ from number–phase uncertainty on the statistical manifold. Preprint.

[61] Glauber RJ. 1963 Coherent and incoherent states of the radiation field. *Phys. Rev.* **131**, 2766–2788.

[62] Sudarshan ECG. 1963 Equivalence of semiclassical and quantum mechanical descriptions. *Phys. Rev. Lett.* **10**, 277–279.

[63] Berger H. 1929 Über das Elektroenkephalogramm des Menschen. *Arch. Psychiatr. Nervenkr.* **87**, 527–570.

[64] Pfurtscheller G, Lopes da Silva FH. 1999 Event-related EEG/MEG synchronization and desynchronization: basic principles. *Clin. Neurophysiol.* **110**, 1842–1857.

[65] Barry RJ, Clarke AR, Johnstone SJ, Magee CA, Rushby JA. 2007 EEG differences between eyes-closed and eyes-open resting conditions. *Clin. Neurophysiol.* **118**, 2765–2773.

[66] Klimesch W, Sauseng P, Hanslmayr S. 2007 EEG alpha oscillations: the inhibition–timing hypothesis. *Brain Res. Rev.* **53**, 63–88.

[67] Wijsman RA. 1973 On the attainment of the Cramér–Rao lower bound. *Ann. Statist.* **1**, 538–542.

[68] Casella G, Berger RL. 2002 *Statistical Inference.* 2nd edn. Pacific Grove, CA: Duxbury.

[69] Cover TM, Thomas JA. 2006 *Elements of Information Theory.* 2nd edn. Hoboken, NJ: Wiley.

[70] Jeffreys H. 1946 An invariant form for the prior probability in estimation problems. *Proc. R. Soc. Lond. A* **186**, 453–461.